February 20, 2010

Leading-Order Determination of the Gluon Polarization from high-p_T Hadron Electroproduction

The HERMES **Collaboration**

ABSTRACT: Longitudinal double-spin asymmetries of charged hadrons with high transverse momentum p_T have been measured in electroproduction using the HERMES detector at HERA. Processes involving gluons in the nucleon have been enhanced relative to others by selecting hadrons with p_T typically above 1 GeV. In this kinematic domain the gluon polarization has been extracted in leading order making use of the model embedded in the Monte Carlo Generator PYTHIA 6.2. The gluon polarization obtained from single inclusive hadrons in the p_T range 1 GeV $< p_T <$ 2.5 GeV using a deuterium target is $\frac{\Delta g}{g}(x,\mu^2)=$ $0.049 \pm 0.034(stat) \pm 0.010(sys\text{-}exp)^{+0.126}_{-0.099}(sys\text{-}models)$ at a scale $\langle \mu^2 \rangle = 1.35$ GeV^2 and $\langle x \rangle = 0.22$. For different final states and kinematic domains, consistent values of $\frac{\Delta g}{g}$ have been found within statistical uncertainties using hydrogen and deuterium targets.

KEYWORDS: Lepton-Nucleon Scattering, Deep Inelastic Scattering, QCD, gluon polarization.

The HERMES Collaboration

A. Airapetian [12,15], N. Akopov [25], Z. Akopov [5], E.C. Aschenauer [6,a],
W. Augustyniak [24], R. Avakian [25], A. Avetissian [25], E. Avetisyan [5],
S. Belostotski [17], N. Bianchi [10], H.P. Blok [16,23], H. Böttcher [6], C. Bonomo [9],
A. Borissov [5], V. Bryzgalov [18], M. Capiluppi [9], G.P. Capitani [10], E. Cisbani [20],
M. Contalbrigo [9], P.F. Dalpiaz [9], W. Deconinck [5,15,b], R. De Leo [2], M. Demey [16]
L. De Nardo [15,5], E. De Sanctis [10], M. Diefenthaler [14,8], P. Di Nezza [10],
J. Dreschler [16] M. Düren [12], M. Ehrenfried [12] G. Elbakian [25], F. Ellinghaus [4,c],
U. Elschenbroich [11] R. Fabbri [6], A. Fantoni [10], L. Felawka [21], S. Frullani [20],
D. Gabbert [11,6], G. Gapienko [18], V. Gapienko [18], F. Garibaldi [20],
G. Gavrilov [5,17,21], V. Gharibyan [25], F. Giordano [5,9], S. Gliske [15], H. Guler [6]
C. Hadjidakis [10,d], M. Hartig [5,e], D. Hasch [10], T. Hasegawa [22], G. Hill [13],
A. Hillenbrand [6], M. Hoek [13], Y. Holler [5], B. Hommez [11], I. Hristova [6],
A. Ivanilov [18], H.E. Jackson [1], R. Kaiser [13], T. Keri [13,12], E. Kinney [4],
A. Kisselev [17], M. Kopytin [6], V. Korotkov [18], P. Kravchenko [17], L. Lagamba [2],
R. Lamb [14], L. Lapikás [16], I. Lehmann [13], P. Lenisa [9], P. Liebing [6,f],
L.A. Linden-Levy [14], W. Lorenzon [15], X.-R. Lu [22] B. Maiheu [11],
N.C.R. Makins [14], B. Marianski [24], H. Marukyan [25], V. Mexner [16],
C.A. Miller [21], Y. Miyachi [22], V. Muccifora [10], M. Murray [13], A. Mussgiller [5,8],
E. Nappi [2], Y. Naryshkin [17], A. Nass [8], M. Negodaev [6], W.-D. Nowak [6],
L.L. Pappalardo [9], R. Perez-Benito [12], N. Pickert [8] M. Raithel [8], D. Reggiani [8]
P.E. Reimer [1], A. Reischl [16] A.R. Reolon [10], C. Riedl [6], K. Rith [8], S.E. Rock [5,g],
G. Rosner [13], A. Rostomyan [5], J. Rubin [1,14], Y. Salomatin [18], A. Schäfer [19],
G. Schnell [6,22], K.P. Schüler [5], B. Seitz [13], C. Shearer [13] T.-A. Shibata [22],
V. Shutov [7], M. Stancari [9], M. Statera [9], J.J.M. Steijger [16], J. Stewart [6]
F. Stinzing [8], S. Taroian [25], B. Tchuiko [18], A. Trzcinski [24], M. Tytgat [11],
A. Vandenbroucke [11] P.B. van der Nat [16] G. van der Steenhoven [16]
Y. Van Haarlem [11,h], C. Van Hulse [11], M. Varanda [5] D. Veretennikov [17],
I. Vilardi [2] C. Vogel [8] S. Wang [3], S. Yaschenko [6,8], H. Ye [3], Z. Ye [5] W. Yu [12],
D. Zeiler [8], B. Zihlmann [11] P. Zupranski [24]

[1] *Physics Division, Argonne National Laboratory, Argonne, Illinois 60439-4843, USA*
[2] *Istituto Nazionale di Fisica Nucleare, Sezione di Bari, 70124 Bari, Italy*

[a]Now at: Brookhaven National Laboratory, Upton, New York 11772-5000, USA

[b]Now at:Massachusetts Institute of Technology, Cambridge, Massachusetts 02139, USA

[c]Now at:Institut für Physik, Universität Mainz, 55128 Mainz, Germany

[d]Now at: IPN (UMR 8608) CNRS/IN2P3 - Université Paris-Sud, 91406 Orsay, France

[e]Now at: Institut für Kernphysik, Universität Frankfurt a.M., 60438 Frankfurt a.M., Germany

[f]Now at: Institute of Environmental Physics and Remote Sensing, University of Bremen, 28334 Bremen, Germany

[g]Present affiliation: SLAC National Accelerator Laboratory, Menlo Park, California 94025, USA

[h]Now at: Carnegie Mellon University, Pittsburgh, Pennsylvania 15213, USA

[3] School of Physics, Peking University, Beijing 100871, China

[4] Nuclear Physics Laboratory, University of Colorado, Boulder, Colorado 80309-0390, USA

[5] DESY, 22603 Hamburg, Germany

[6] DESY, 15738 Zeuthen, Germany

[7] Joint Institute for Nuclear Research, 141980 Dubna, Russia

[8] Physikalisches Institut, Universität Erlangen-Nürnberg, 91058 Erlangen, Germany

[9] Istituto Nazionale di Fisica Nucleare, Sezione di Ferrara and Dipartimento di Fisica, Università di Ferrara, 44100 Ferrara, Italy

[10] Istituto Nazionale di Fisica Nucleare, Laboratori Nazionali di Frascati, 00044 Frascati, Italy

[11] Department of Subatomic and Radiation Physics, University of Gent, 9000 Gent, Belgium

[12] Physikalisches Institut, Universität Gießen, 35392 Gießen, Germany

[13] Department of Physics and Astronomy, University of Glasgow, Glasgow G12 8QQ, United Kingdom

[14] Department of Physics, University of Illinois, Urbana, Illinois 61801-3080, USA

[15] Randall Laboratory of Physics, University of Michigan, Ann Arbor, Michigan 48109-1040, USA

[16] National Institute for Subatomic Physics (Nikhef), 1009 DB Amsterdam, The Netherlands

[17] Petersburg Nuclear Physics Institute, Gatchina, Leningrad region 188300, Russia

[18] Institute for High Energy Physics, Protvino, Moscow region 142281, Russia

[19] Institut für Theoretische Physik, Universität Regensburg, 93040 Regensburg, Germany

[20] Istituto Nazionale di Fisica Nucleare, Sezione Roma 1, Gruppo Sanità and Physics Laboratory, Istituto Superiore di Sanità, 00161 Roma, Italy

[21] TRIUMF, Vancouver, British Columbia V6T 2A3, Canada

[22] Department of Physics, Tokyo Institute of Technology, Tokyo 152, Japan

[23] Department of Physics, VU University, 1081 HV Amsterdam, The Netherlands

[24] Andrzej Soltan Institute for Nuclear Studies, 00-689 Warsaw, Poland

[25] Yerevan Physics Institute, 375036 Yerevan, Armenia

1. Introduction

In recent years a major goal in the study of Quantum Chromo-Dynamics (QCD) has been the detailed investigation of the spin structure of the nucleon and the determination of the partonic composition of its spin projection [1]

$$\frac{1}{2} = S_z = \frac{1}{2} \cdot \Delta\Sigma + \Delta G + L_z^q + L_z^G. \tag{1.1}$$

Here $\Delta\Sigma$ is the contribution of the quark and anti-quark helicities, ΔG is the contribution of the gluon helicity, and L_z^q and L_z^G are the quark and gluon orbital angular momenta, respectively, in a reference system where the nucleon has very large longitudinal momentum. The individual terms in the sum depend on the scale μ^2 and the renormalization scheme. Recent results from experiments [2, 3] and fits in next-to-leading order (NLO) QCD [4, 5, 6, 7] to helicity-dependent inclusive Deep-Inelastic Scattering (DIS) data [2, 8, 9, 10, 11, 12, 13, 14, 15, 16, 17, 18] yield a value of $\Delta\Sigma \sim 0.2 - 0.4$ at $\mu^2 = 4$ GeV^2 in the $\overline{\text{MS}}$ scheme [19]. In contrast to the quark helicity distributions, the knowledge of the gluon helicity distribution function is still limited. There are no direct experimental determinations of parton orbital angular momenta. Most of the existing knowledge about $\Delta G(\mu^2)$ originates from next-to-leading order perturbative QCD (pQCD) fits to the helicity-dependent structure function $g_1(x_B, Q^2)$ of the nucleon, where x_B is the Bjorken scaling variable, which is in leading-order (LO) identified with the longitudinal parton momentum fraction x in the nucleon. In DIS the renormalization and factorization scales μ^2 are set equal to the photon virtuality Q^2. Because the virtual photon does not couple directly to gluons (see Fig. 1b), $g_1(x_B, Q^2)$ is only weakly sensitive to gluons through the DGLAP evolution [20, 21, 22] of the helicity-dependent Parton Distribution Functions (PDFs). At next-to-leading order pQCD, additional sensitivity to gluons arises from the Photon-Gluon Fusion (PGF) subprocess (see Fig. 1b). However, the limitations on the precision and kinematic range in x_B and Q^2 of the g_1 measurements result in large experimental and theoretical uncertainties on the determination of the gluon helicity distribution function $\Delta g(x, \mu^2)$. Results for $\Delta G(\mu^2) = \int_0^1 \Delta g(x, \mu^2) dx$ from recent pQCD fits to inclusive DIS data [4, 5, 6, 7] are typically of order 0.5 with uncertainties up to ± 1.

An alternative constraint on the extraction of $\Delta G(\mu^2)$ in NLO pQCD fits comes from the measurements of double-spin asymmetries in production of inclusive π^0 mesons or jets with high transverse momentum in polarized proton-(anti-)proton scattering. First measurements were performed by E704 [23] and more recent data were obtained by PHENIX [24] and STAR [25] at RHIC. The inclusion of the RHIC-data in recent NLO pQCD fits [6] improves the accuracy on Δg significantly. One finds $|\Delta g(x, Q^2)|$ smaller than 0.1, with a possible node in the distribution. This is driven mainly by the RHIC data, which constrain the magnitude of $\Delta g(x)$ for $0.05 < x < 0.2$, but cannot determine its sign as they mainly probe the product of the gluon helicity distribution at two x values.

In order to increase the sensitivity to $\Delta g(x, \mu^2)$ in lepton-nucleon scattering, other observables besides the inclusive helicity-dependent structure function have been studied. These observables are expected to include a direct contribution from gluons. For example,
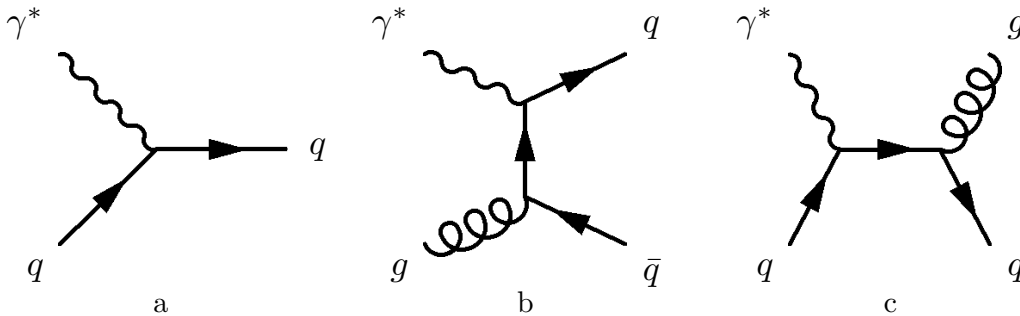
Figure 1: Feynman diagrams for hard subprocesses: a) $\mathcal{O}(\alpha_s^0)$ DIS, b) $\mathcal{O}(\alpha_s^1)$ Photon-Gluon Fusion, and c) $\mathcal{O}(\alpha_s^1)$ QCD Compton scattering.

in hadron leptoproduction this gluonic contribution can be relatively enhanced by detecting charmed hadrons, or inclusive hadrons or hadron pairs at high transverse momenta p_T.

Charmed hadron electroproduction is a suitable channel because it is dominated by the PGF subprocess [26] and a hard scale is introduced by the mass of the charm-quark pair, which makes pQCD calculations of this process possible. For light final state quarks, the selection of hadrons with high p_T enhances the relative contribution of the gluon subprocesses and the relevant transverse momenta provide the scale (see Sect. 5.3). In the high p_T domain other calculable hard pQCD subprocesses such as QCD Compton (QCDC) scattering (see Fig. 1c) are relatively enhanced as well, whereas soft, non-perturbative processes are suppressed. Charm electroproduction is being investigated by COMPASS [26, 27]. Inclusive single hadron leptoproduction was studied by E155 [28]. Hadron-pair leptoproduction at high p_T was studied by HERMES [29], SMC [30] and COMPASS [31, 32]. For these experiments high p_T is in the range from one to a few GeV.

Throughout this paper, the term "LO" is applied to all leading order subprocesses contributing to hadron production at nonzero p_T. These are the tree level processes at $\mathcal{O}(\alpha_s^1)$, but also the quark scattering process $\gamma^* q \to q$ (DIS) at $\mathcal{O}(\alpha_s^0)$. While the former processes involve hard gluons, and can therefore involve substantial parton transverse momentum $\hat{p}_T$ in the hard scattering, in the latter process $\hat{p}_T$ is equal to zero, but hadrons acquire p_T from soft initial and final state radiation. This paper presents the LO extraction of the gluon polarization $\frac{\Delta g}{g}(x)$ from longitudinal double-spin asymmetries of charged inclusive hadrons measured in electroproduction using a deuterium target by HERMES at HERA. The contributions of signal and background have been determined by a PYTHIA Monte Carlo simulation, which includes LO pQCD as well as non-perturbative subprocesses. Consistency checks have been performed for different kinematic regions, different final states and using data from a hydrogen target. The data taken with the deuterium target correspond to an integrated luminosity three times larger than that taken with the hydrogen target, see table 1. Compared to the previous HERMES publication [29], which used measurements of hadron pairs of opposite charge, this analysis involves a much larger sample of single hadrons, and a significantly more comprehensive treatment of the underlying physics processes [33, 34]. Therefore, the results presented here supersede those of Ref. [29].

This paper is organized as follows: In Sect. 2 the experimental method is described, in Sect. 3 the asymmetry results are given, in Sect. 4 the determination of $\frac{\Delta g}{g}$ with a description of the physics model of the reactions is discussed, in Sect. 5 the PYTHIA Monte Carlo simulation is described, in Sect. 6 the determination of $\frac{\Delta g}{g}(x, \mu^2)$ is explained, and in Sect. 7 the summary and conclusions are given.

2. The HERMES Experiment

Positrons of momentum 27.6 GeV were stored in the HERA lepton ring at DESY. The initially unpolarized beam was transversely polarised by an asymmetry in the emission of synchrotron radiation associated with a spin flip (Sokolov-Ternov mechanism [35]). The polarization was rotated to the longitudinal direction for passage through an gaseous internal fixed target of longitudinally nuclear-polarized atoms. The scattered positron and hadrons produced were detected in a forward magnetic spectrometer. The beam helicity was reversed periodically. The beam polarization was measured continuously by two independent polarimeters using Compton backscattering of circularly polarized laser light [36, 37]. The average beam polarization for the data used in this analysis is shown in Tab. 1. The target [38] consisted of longitudinally nuclear-polarized pure atomic hydrogen or deuterium gas in an open-ended 40 cm long storage cell. The cell was fed by an atomic-beam source based on Stern-Gerlach separation combined with radio-frequency transitions of atomic hyperfine states [39]. The sign of the nuclear polarization of the atoms was chosen randomly every 60 s (90 s) for the hydrogen (deuterium) target. The polarization and the atomic fraction inside the target cell were continuously measured [40, 41]. The average values of the target polarization for both hydrogen and deuterium data are shown in Tab. 1. The luminosity was measured by detecting e^+e^- pairs originating from Bhabha scattering of the beam positrons off electrons in the target atoms, and also $\gamma\gamma$ pairs from e^+e^- annihilations [42].

Year	Target	Luminosity pb^{-1}	Average Beam Polarization	Average Target Polarization
1996	H	12.6	0.528 ± 0.018	0.759 ± 0.032
1997	H	37.3	0.531 ± 0.018	0.851 ± 0.032
2000	D	138.7	0.533 ± 0.010	0.846 ± 0.030

Table 1: Integrated luminosities, average beam and target polarizations for the data used in this analysis.

The HERMES spectrometer [43] consisted of two identical halves separated by a horizontal flux diversion plate, which limited the minimum detected angle. The geometrical acceptance was ± 170 mrad in the horizontal (bending) plane and between $\pm(40-140)$ mrad in the vertical plane resulting in a range of polar angles between 40 mrad and 220 mrad. Each half was instrumented with 3 planes of hodoscopes, 36 planes of drift chambers, and 9 planes of proportional chambers. The particle identification system consisted of an electromagnetic calorimeter, a pre-shower hodoscope, a transition-radiation detector, and a Čerenkov detector. Detailed descriptions of these components can be found in

Refs. [43, 44, 45, 46, 47, 48]. Positrons within the acceptance could be separated from hadrons with an efficiency exceeding 98% and a hadron contamination of less than 1%.

The main HERMES physics trigger was formed by a coincidence of hits in the hodoscopes in the front and back regions of the spectrometer with the requirement of an energy deposit above 1.4 GeV in the calorimeter. This trigger was almost 100% efficient for positrons with energies above threshold. Events with no positron in the acceptance were recorded using a mixture of the main trigger and another trigger formed by a coincidence between the hodoscopes and two tracking planes, requiring that there is at least one charged track. The influence of trigger efficiencies on the analysis has been studied in [33].

3. Experimental Results

The ratio $\frac{\Delta g}{g}(x, \mu^2)$ of helicity-dependent to helicity-averaged gluon distributions, *i.e.* the gluon polarization, is determined by measuring the double-spin cross section asymmetry of one or two high-p_T inclusive hadrons produced in the scattering of longitudinally polarized positrons incident on the longitudinally polarized target. The definitions of the kinematic variables in electroproduction used in this paper are shown in Tab. 2. The longitudinal double-spin cross section asymmetry is given by the ratio of helicity-dependent to helicity-averaged cross sections $A = \Delta\sigma/(2\sigma)$, where $\sigma = (\sigma^{\overrightarrow{\Leftarrow}} + \sigma^{\overrightarrow{\Rightarrow}})/2$, $\Delta\sigma = \sigma^{\overrightarrow{\Leftarrow}} - \sigma^{\overrightarrow{\Rightarrow}}$, and the single (double) arrows denote the relative alignment of longitudinal spins of the lepton (nucleon) with respect to the lepton beam direction.

The data for this analysis were collected in 1996, 1997, and 2000 (see Tab. 1). The analysis presented in this paper includes all (unidentified) charged hadrons. Separate asymmetries are given for each charge, target, and event category.

3.1 Event categories

Simulations indicate that subprocesses involving hard gluons are relatively enhanced by measuring hadrons with high p_T with respect to the virtual photon direction ($p_{T(\gamma^*)}$). Correlations between hadrons in an event may also enhance the signal. Events are categorized by the number of hadrons observed in an event and whether kinematic information on the scattered positron is available or not. Each possible combination of two hadrons is counted as a separate event in the pairs category. The categories are defined in detail as follows:

- **'anti-tagged' single inclusive hadrons:** The scattered positron was not detected. The hadron transverse momentum $p_{T(beam)}$ was measured with respect to the beam direction as the direction of the virtual photon is unknown. In most cases, the undetected positron had a small scattering angle (and hence Q^2 is small) and stayed inside the beam pipe. The difference between $p_{T(beam)}$ and $p_{T(\gamma^*)}$ is then very small. However, the positron could also escape the detector acceptance because of a large scattering angle, in which case Q^2 was large. The large angle of the virtual photon with respect to the beam axis results in a significantly larger $p_{T(beam)}$ than $p_{T(\gamma^*)}$ of the hadron. Although these events with large Q^2 are rare, they can account for a significant fraction of the hadrons at high $p_{T(beam)}$. For $p_T > 1.0$ GeV the deuteron (proton) data sample in this category contains 1272k (419k) hadrons.

$k = (E, \vec{k})$, $k' = (E', \vec{k'})$	4–momenta of the initial and final state leptons
θ, ϕ	Polar and azimuthal angle of the scattered positron
M	Mass of the initial target nucleon
$q = (E - E', \vec{k} - \vec{k'})$	4–momentum of the virtual photon
$Q^2 = -q^2 \overset{\text{lab}}{\approx} 4EE' \sin^2 \frac{\theta}{2}$	Negative squared 4-momentum transfer
$\nu = \frac{P \cdot q}{M} \overset{\text{lab}}{=} E - E'$	Energy of the virtual photon
$x = \frac{Q^2}{2\,P \cdot q} \overset{\text{lab}}{=} \frac{Q^2}{2\,M\nu}$	Bjorken scaling variable
$y = \frac{P \cdot q}{P \cdot k} \overset{\text{lab}}{=} \frac{\nu}{E}$	Fractional energy of the virtual photon
$W^2 = (P + q)^2$ $\overset{\text{lab}}{=} M^2 + 2M\nu - Q^2$	Squared invariant mass of the virtual-photon nucleon system
$p = (E_h, \vec{p})$	4-momentum of a hadron in the final state
p_T	Transverse momentum of a hadron
$p_{T(\gamma^*)}$	p_T with respect to the virtual photon
$p_{T(beam)}$	p_T with respect to the incoming positron
p_T^{frag}	Transverse hadron momentum from fragmentation
$\sum p_{T(beam)}^2$	For two hadrons: $(p_T^{h1})^2 + (p_T^{h2})^2$
$z = \frac{P \cdot P_h}{P \cdot q} \overset{\text{lab}}{=} \frac{E_h}{\nu}$	Fractional energy of the final state hadron
x	Parton momentum fraction
$\hat{s} = (p_a + p_b)^2$	Mandelstam variable for partonic process $ab \to cd$
$\hat{t} = (p_a - p_c)^2$	Mandelstam variable for partonic process $ab \to cd$
$\hat{u} = (p_b - p_c)^2$	Mandelstam variable for partonic process $ab \to cd$
μ^2	pQCD scale
$\hat{Q}^2$	Scale of the partonic hard subprocess
$\hat{p}_T \; (= \sqrt{\frac{\hat{u}\hat{t}}{\hat{s}}} \;$ for $m = 0)$	Transverse momentum of final state partons in the CM-system of the hard subprocess
k_T	Intrinsic transverse momentum of partons in the nucleon and photon

Table 2: Definition of kinematic variables.

- **'tagged' single inclusive hadrons:** The scattered positron has been detected with $Q^2 > 0.1$ GeV^2, $W^2 > 4$ GeV^2, and $y < 0.95$. The hadron transverse momentum $p_{T(\gamma^*)}$ is measured with respect to the virtual photon direction. For $p_T > 1$ GeV this deuteron (proton) data sample contains 53k (19k) hadrons.

- **inclusive pairs of hadrons:** The hadron pair sample consists of all pairs of charged hadrons with $p_{T(beam)} > 0.5$ GeV. The transverse momentum $p_{T(beam)}$ is measured with respect to the beam direction, because only in 10% of the events the positron was detected. With the additional requirement $\sum p_{T(beam)}^2 > 2.0$ GeV^2 the deuteron (proton) data sample contains 60k (20k) hadron pairs. With this requirement applied, 6% of the anti-tagged inclusive hadrons with $p_{T(beam)} > 1.0$ GeV are contained within the pairs sample.

For all three categories, HERMES data are available for various combinations of target and/or hadron charge detected. As the samples differ in the hard subprocess and final state kinematics and fractions of contributing subprocesses, the corresponding results for the gluon polarization $\frac{\Delta g}{g}(x, \mu^2)$ provide a measure of the consistency of the extraction. The final result for $\frac{\Delta g}{g}(x, \mu^2)$ is obtained from the anti-tagged inclusive hadrons originating from a deuterium target. The other data samples have too small a statistical power to justify carrying out the extensive analysis needed to obtain the systematic uncertainties.

3.2 Asymmetry results

The double-spin asymmetry measured is given by

$$A_{meas} \equiv A_{||} = \frac{N^{\rightleftarrows}L^{\rightrightarrows} - N^{\rightrightarrows}L^{\rightleftarrows}}{N^{\rightleftarrows}L_P^{\rightrightarrows} + N^{\rightrightarrows}L_P^{\rightleftarrows}}. \tag{3.1}$$

Here $N^{\rightrightarrows}$ ($N^{\rightleftarrows}$) is the number of hadrons or hadron pairs for target spin orientation parallel (anti-parallel) to the beam spin orientation, $L^{\rightrightarrows}$ ($L^{\rightleftarrows}$) is the corresponding integrated luminosity, and $L_P^{\rightrightarrows}$ ($L_P^{\rightleftarrows}$) is the product of luminosity and live time fraction convoluted over time with the absolute values of beam and target polarizations. There is a small background ($< 0.1\%$) from positrons misidentified as hadrons (and vice versa). In the tagged category a correction was applied for an approximately 5% contribution of positrons originating from charge-symmetric processes.

The asymmetries for the anti-tagged and tagged categories are shown as a function of transverse momentum in Figs. 2 and 3, respectively, and listed in tables 9 - 10. The asymmetry of the pairs is presented as a function of the minimum requirement, $(\sum p_{T(beam)}^2)_{min}$, in Fig. 4 and in table 11. The considerably different values of the asymmetries in the different categories, charges and targets are due to the different underlying mixtures of subprocesses and of quark content, as discussed in Sect. 5.3.

The curves in Figs. 2, 3, and 4 show the asymmetries calculated by the procedure discussed in Sect. 4 using the values $\frac{\Delta g}{g}(x, \mu^2) = -1, 0, +1$ (from top to bottom). They illustrate the sensitivity of the HERMES data to $\frac{\Delta g}{g}(x, \mu^2)$. The data are close to the central curve indicating small average values of $\frac{\Delta g}{g}$.

4. Physics Model

4.1 Subprocesses

Both the helicity-averaged and helicity-dependent cross sections include contributions from hard subprocesses that can be calculated using pQCD and from soft subprocesses such as those described by the Vector-Meson Dominance (VMD) model (see Fig. 1). A smooth transition from soft subprocesses to hard subprocesses is regulated by a set of cutoff parameters (for details [33, 49, 50, 51]). The measured asymmetry is the weighted sum of the asymmetries of all subprocesses. When it is impossible to reliably separate the subprocesses experimentally, as in fixed-target experiments, the fractions of events originating from the
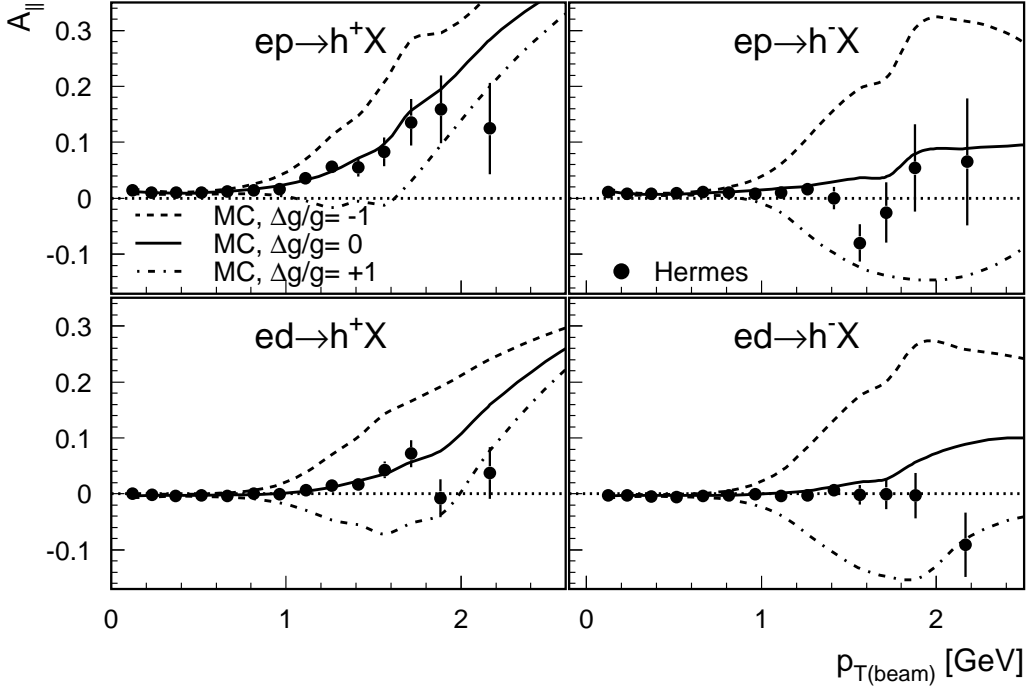
Figure 2: Measured asymmetry for the anti-tagged category of events for positive (left) and negative (right) inclusive hadrons from hydrogen (top) and deuterium (bottom) targets as a function of $p_{T(beam)}$. The uncertainties are statistical only. There is an overall normalization uncertainty of 5.2% (3.9%) for hydrogen (deuterium). The curves show the Monte Carlo asymmetries for three different fixed values assumed for the gluon polarization.

different subprocesses must be modeled. In the analysis described in this paper, this is done using the **spin independent** Monte Carlo (MC) program PYTHIA 6.2 [49, 50, 51].

The various subprocesses are classified in terms of the model used in PYTHIA. In this model, the wave function of the incoming photon has three components, a "VMD", a "direct" and an "anomalous" one. The generic photon processes following from this decomposition are depicted in Fig. 5. The direct photon interacts as a point-like particle with the partons of the nucleon, while the VMD and anomalous components interact through their hadronic structure.

Figure 5b shows an example of a direct process. The direct pQCD subprocesses studied in this analysis are the $\mathcal{O}(\alpha_s^0)$ DIS process (Fig. 1a), the $\mathcal{O}(\alpha_s^1)$ processes PGF (Fig. 1b), and QCDC (Fig. 1c).

The VMD component is characterized by small-scale, non-perturbative fluctuations of the photon into a $q\bar{q}$ pair existing long enough to evolve into a hadronic state before the interaction with the nucleon. This process can be described in the framework of the VMD model, where the hadronic state is treated as a vector meson (*e.g.*, ρ^0, ω, ϕ) with the same quantum numbers as the photon. Higher-mass and non-resonant states are added in the Generalized VMD (GVMD) model. The (G)VMD hadronic states can undergo all the interactions with the nucleon allowed in hadronic physics, *i.e.*, elastic and diffractive as well as inelastic non-diffractive reactions. The latter can be either soft ("low-p_T") processes or
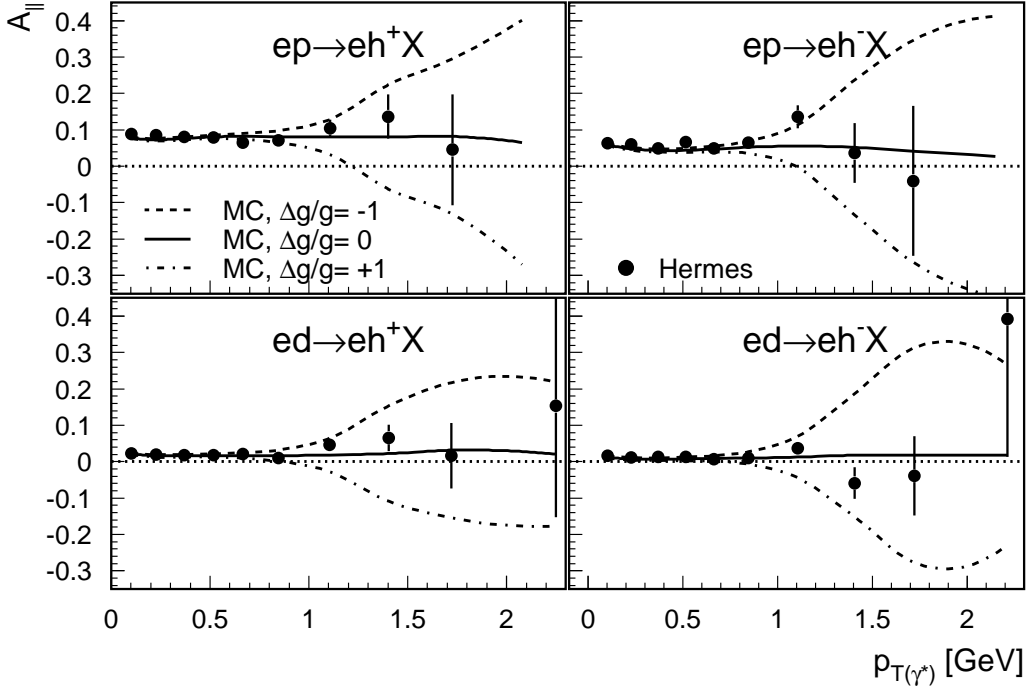
Figure 3: Measured asymmetry for the tagged category of events for positive (left) and negative (right) inclusive hadrons from hydrogen (top) and deuterium (bottom) targets as a function of $p_{T(\gamma^*)}$. The uncertainties are statistical only. There is an overall experimental normalization uncertainty of 5.2% (3.9%) for hydrogen (deuterium). The curves show the Monte Carlo asymmetries for three different fixed values assumed for the gluon polarization.
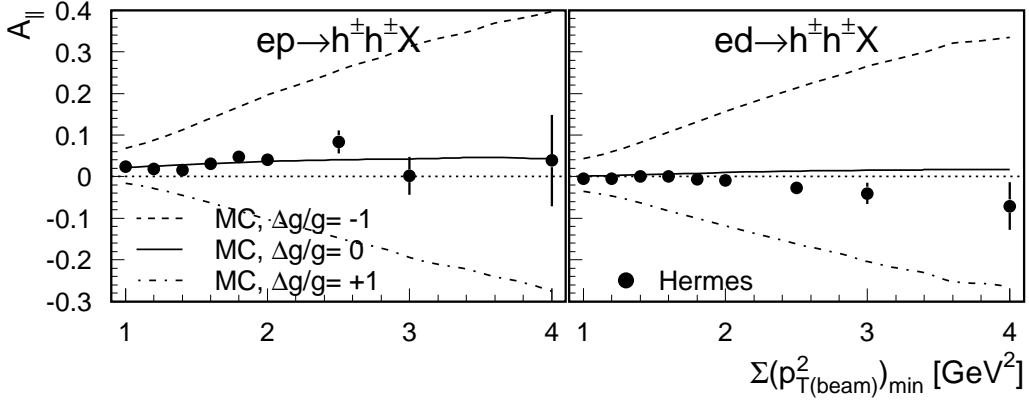
Figure 4: Measured asymmetry for hadron pairs produced from hydrogen (left) and deuterium (right) targets as a function of the minimum value of $\sum p_{T(beam)}^2$. The uncertainties are statistical only. There is an overall experimental normalization uncertainty of 5.2% (3.9%) for hydrogen (deuterium). The curves show the Monte Carlo asymmetries for three different values assumed for the gluon polarization.

hard QCD $2 \to 2$ processes. A generic example of a VMD process is shown in Fig. 5a .

The anomalous photon is characterized by sufficiently large-scale, perturbative fluctuations of the photon into a $q\bar{q}$ pair. The allowed processes are the same pQCD $2 \to 2$
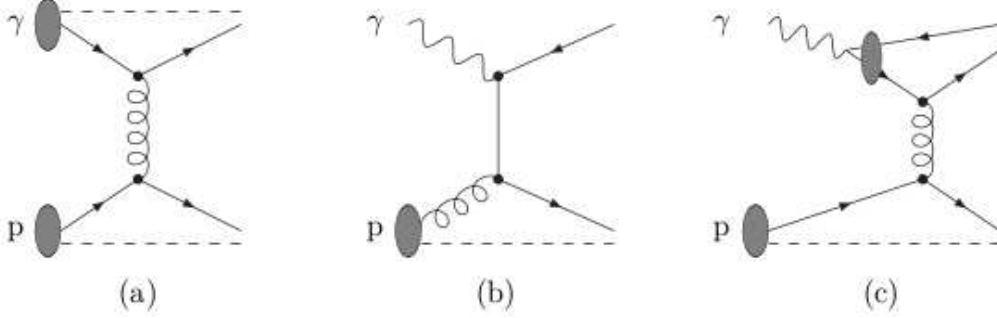
Figure 5: Contributions to hard p interactions: (a) VMD, (b) direct, and (c) anomalous. Only the basic graphs are illustrated; additional partonic activity is allowed in all three processes. The presence of spectator jets has been indicated by dashed lines, while full lines show partons that (may) give rise to high-p_t jets. The gray ovals represent multiparton wave functions. Anomalous states are built up from a perturbatively given $q\bar{q}$ fluctuation, while VMD fluctuations allow no simple perturbative representation; hence the difference in the placing of the ovals [51].

processes as in the hard VMD case, with the difference that for the anomalous component the parton distributions of the photon are relevant, whereas for the description of the hard VMD component those of the vector meson are used. Both hard VMD and anomalous components are usually referred to as "resolved" photons. Depending on whether a quark or a gluon in the nucleon is struck by a resolved photon the corresponding hard subprocesses are labeled by a 'q' or 'g' in this paper. A generic example of an anomalous process is shown in Fig. 5c. The resolved-photon processes are of $\mathcal{O}(\alpha_s^1)$ with a hidden $1/\alpha_s(\mu^2)$ term in the evolution of the photon's parton distributions canceling the additional vertex [52].

For hard subprocesses the nucleon is described by helicity-averaged (helicity-dependent) PDFs, which are the average (difference) of the number densities of partons of type f whose spins are aligned, f^+, those whose spins are anti-aligned, f^-, with respect to the nucleon spin: $f(x,\mu^2){=}f^+(x,\mu^2) + f^-(x,\mu^2)$ $(\Delta f(x,\mu^2){=}f^+(x,\mu^2) - f^-(x,\mu^2))$, where f$=$ u, d, s, or g. The integral over x, $\Delta f(\mu^2) = \int_0^1 dx \Delta f(x,\mu^2)$, gives the total spin contribution of the respective partons to the nucleon spin, as used in Eq. 1.1. The hard part of the single-inclusive differential helicity-dependent cross section for the process $\gamma^* p \to hX$ can be expressed as an integral over the parton distribution functions, the hard partonic cross sections for the subprocesses $ab \to cX$, and the fragmentation functions. It can be written schematically as

$$d\Delta\sigma^{\gamma^* p \to hX} = \sum_{a,b,c=q,\bar{q},g} \int dx_a dx_b dz_c \Delta f_a^{\gamma^*}(x_a,\mu^2) \Delta f_b^N(x_b,\mu^2)$$
$$\times d\Delta\hat{\sigma}^{ab \to cX}(\hat{s},\hat{t},\mu^2,Q^2) D_c^h(z_c,\mu^2) , \tag{4.1}$$

and correspondingly for the helicity-averaged cross section and distributions. Here x_b is the fraction of the nucleon momentum carried by parton b and $f_b^N(x_b,\mu^2)$ $(\Delta f_b^N(x_b,\mu^2))$ is the corresponding nucleon PDF. Similarly x_a is the fraction of the photon momentum carried by parton a, and $f_a^{\gamma^*}(x_a,\mu^2)$ $(\Delta f_a^{\gamma^*}(x_a,\mu^2))$ is the corresponding photon PDF. For the direct-photon processes a equals γ^* and $f_a^{\gamma^*}(x_a,\mu^2)$ $(\Delta f_a^{\gamma^*}(x_a,\mu^2))$ reduces to $\delta(1-x_a)$. The

fragmentation function $D_c^h(z_c, \mu^2)$ describes the hadronization of a parton c into a hadron h with a momentum $p_h = z_c p_c$. The hard partonic cross section $d\hat{\sigma}^{ab \to cX}(\hat{s}, \hat{t}, \mu^2, Q^2)$ $(d\Delta\hat{\sigma}^{ab \to cX}(\hat{s}, \hat{t}, \mu^2, Q^2))$ depends on the subprocess kinematics, the renormalization and factorization scales, and on Q^2 in case of the direct-photon processes. Here, $\hat{s}$ and $\hat{t}$ are the Mandelstam variables for the partonic interaction, which are related to x_a and x_b. More information on the kinematic variables is given in table 2. The cross section for hadron pairs $d\sigma^{\gamma^* p \to h_1 h_2 X}$ $(d\Delta\sigma^{\gamma^* p \to h_1 h_2 X})$ can be obtained analogously to Eq. 4.1.

The cross sections and asymmetries of the soft VMD interactions can only be modeled phenomenologically. The PYTHIA model incorporates the total γp and hadronic cross section parameterizations of Donnachie and Landshoff [53] together with quark counting rules [54, 55]. This model successfully describes the measured total, elastic, and diffractive cross sections over a wide energy range. The non-diffractive cross section is modeled in PYTHIA as the difference of the total cross section and the summed elastic and diffractive cross sections; the corresponding subprocess is called "low-p_T". The PYTHIA model provides a smooth transition from real to virtual photons and is applicable from very small to large values of Q^2. It uses a number of cutoff, scale, and suppression parameters together with several possible prescriptions on how to use them to select the underlying subprocess of an event. The default prescriptions and the cutoff and scale parameters were developed and tuned to match high energy data. In this application to the lower energy of HERMES the influence of various prescriptions and parameter values has been carefully studied (see Sects. 5 and 6.4).

Table 3 shows a compilation of the modeled reactions, the corresponding PYTHIA subprocess numbers, their classification, description, and name used in this paper.

4.2 Signal and Background Asymmetries

In the simulation, the cross section is considered to arise from an *incoherent* superposition of all contributing subprocess amplitudes. The kinematic selection criteria (*e.g.*, event category and hadron p_T) for the Monte Carlo are the same as those for the data. PYTHIA events are generated independent of helicity, therefore the MC asymmetry A_{MC} is calculated by weighting each selected MC generated hadron with the calculated event asymmetry w_k. The average of these weights is A_i, the asymmetry for subprocess i

$$A_i = \frac{1}{N_i} \sum_{k=1}^{N_i} w_k, \tag{4.2}$$

where N_i is the number of entries. The event-by-event weighting method guarantees the correct integration over the subprocess kinematics, and all partons in the nucleon and the photon (where applicable). The Monte Carlo asymmetry A_{MC} is the sum of the asymmetries from signal (A_{MC}^{SIG}) and background (A_{MC}^{BG}) subprocesses weighted by their fraction of entries R^{SIG} and R^{BG}. It is given by

$$A_{MC}(p_T) = R^{BG} A_{MC}^{BG}(p_T) + R^{SIG} A_{MC}^{SIG}(p_T) = \sum_{i \in BG} R_i A_i + \sum_{i \in sig} R_i A_i, \tag{4.3}$$

Subprocess	#	Class	Description	Name
soft VMD				
$VN \to VN$	91	background	elastic VMD	exclusive VMD
$VN \to VX$	92	background	single-diffractive VMD	
$VN \to XN$	93	background	single-diffractive VMD	
$VN \to XX$	94	background	double-diffractive VMD	
$VN \to X$	95	background	soft non-diffractive VMD	low-p_T
RESOLVED (hard VMD and anomalous)				
$qq \to qq$	11	background	QCD $2 \to 2$	QCD $2 \to 2(q)$
$q\bar{q} \to q\bar{q}$	12	background	.	.
$q\bar{q} \to gg$	13	background	.	.
$gq \to gq$	28	background	.	.
$qg \to qg$	28	signal	.	QCD $2 \to 2(g)$
$gg \to q\bar{q}$	53	signal	.	.
$gg \to gg$	68	signal	.	.
DIRECT				
$\gamma^* q \to q$	99	background	LO DIS	DIS
$\gamma_T^* q \to qg$	131	background	(transverse) QCDC	QCDC
$\gamma_L^* q \to qg$	132	background	(longitudinal) QCDC	.
$\gamma_T^* g \to q\bar{q}$	135	signal	(transverse) PGF	PGF
$\gamma_L^* g \to q\bar{q}$	136	signal	(longitudinal) PGF	.

Table 3: Description of the subprocesses used in this paper. Columns from left to right: subprocess, PYTHIA subprocess number, classification as signal or background, description, and name used in this paper. A vector meson is denoted by V.

where R_i is the fraction of entries from the subprocess i calculated in the PYTHIA simulation. Background processes are all subprocesses that do not involve a hard gluon from the initial nucleon. These include all soft processes, the direct processes DIS and QCDC, and all resolved pQCD processes, which involve a quark or antiquark in the nucleon, *i.e.*, QCD $2 \to 2(q)$. They are listed in Tab. 3. All subprocesses involving a hard gluon of the nucleon in the initial state are considered to be signal processes, *i.e.*, PGF and the hard $2 \to 2(g)$ processes.

The event-by-event weight w for hard subprocesses is given by

$$w = \hat{a}(\hat{s}, \hat{t}, \hat{Q}^2, Q^2) \cdot \frac{\Delta f_a^{\gamma^*}(x_a, \hat{Q}^2)}{f_a^{\gamma^*}(x_a, \hat{Q}^2)} \cdot \frac{\Delta f_b^N(x_b, \hat{Q}^2)}{f_b^N(x_b, \hat{Q}^2)}, \tag{4.4}$$

where $\Delta f_a^{\gamma^*}/f_a^{\gamma^*} = 1$ for $x_a = 1$, *i.e.*, direct photon processes. The hard subprocess asymmetry is $\hat{a}(\hat{s}, \hat{t}, \mu^2) = \Delta\hat{\sigma}/(2\hat{\sigma})$. The lowest order equations for important hard subprocess asymmetries are compiled in appendix A. The VMD and GVMD diffractive subprocesses may have small asymmetries at HERMES energies [56, 57, 58, 59]. The asymmetry of the low-p_T process was estimated from the measured asymmetries and found to be non-zero (see Sect. 5.3). In both cases, the virtual-photon depolarization factor $D(y, Q^2)$ (see

Eq. A.15) has to be applied to the weight in order to account for the transformation of the virtual-photon nucleon asymmetry into a lepton-nucleon asymmetry. The asymmetry from signal subprocesses depends on the unknown $\frac{\Delta g}{g}(x, \mu^2)$ averaged over the subprocess kinematics in the specified p_T range. It can be written as

$$
\begin{aligned}
A_{MC}^{SIG}(p_T) &= \frac{1}{N^{SIG}} \sum_{k=1}^{N^{SIG}} w_k \\
&= \left\langle \hat{a}(\hat{s}, \hat{t}, \hat{Q}^2, Q^2) \cdot \frac{\Delta f_a^{\gamma^*}(x_a, \hat{Q}^2)}{f_a^{\gamma^*}(x_a, \hat{Q}^2)} \cdot \frac{\Delta g}{g}(x_b, \hat{Q}^2) \right\rangle_{(p_T)}^{SIG},
\end{aligned}
\qquad (4.5)
$$

where N^{SIG} is the number of entries from all signal processes. The extraction of the quantity of interest, $\frac{\Delta g}{g}(x, \mu^2)$, is based on Eq. 4.5 replacing the unknown asymmetry $A_{MC}^{SIG}(p_T)$ by

$$
A^{SIG}(p_T) = \frac{A_{meas}(p_T) - R^{BG} A_{MC}^{BG}(p_T)}{R^{SIG}}.
\qquad (4.6)
$$

In Sect. 6 methods will be described to extract $\frac{\Delta g}{g}$ from the right hand side of Eq. 4.5.

5. Monte Carlo simulation

The relevant subprocess cross sections have been modeled by the PYTHIA Monte Carlo program, which uses JETSET [60] for describing the fragmentation process. The standard helicity-averaged input PDFs used are CTEQ5L [61] for the nucleon and Schuler and Sjöstrand [62] for the photon. The scale μ^2 of the $2 \to 2$ subprocesses is defined to be $\mu^2 = \hat{p}_T^2 + \frac{1}{2} Q^2$ (also commonly referred to as $\hat{Q}^2$). Electromagnetic radiative effects [63, 64] have been added to PYTHIA and they constitute a relatively small correction for hadron production at HERMES kinematics [33]. Events generated by PYTHIA are passed through a complete GEANT 3 [65] simulation of the HERMES spectrometer.

5.1 Monte Carlo tuning

In order to account for the relatively low center-of-mass energy of the HERMES experiment several parameters in the event generation were adjusted and the model describing exclusive vector meson production was improved [33]. This was done in the kinematic region of the tagged events because more kinematic variables are measured for this category than for the anti-tagged category. The tuning of the fragmentation parameters [66] was performed using a subsample with $p_{T(\gamma^*)} < 0.8$ GeV and $Q^2 > 1$ GeV^2 where the DIS process (Fig. 1a) is dominant and NLO corrections are small. The values of the adjusted parameters, shown in Tab. 7 in appendix B, are used for all event categories.

Figure 6 shows the measured and the simulated cross sections as a function of x_B, Q^2, and z for the tagged category of events using a deuterium target. Both the simulated and measured cross sections are not corrected for acceptance effects. These cross sections vary over more than three orders of magnitude. The data and MC simulation agree to within 15% for $x_B < 0.2$, where most of the data reside for the tagged event category. Thus in
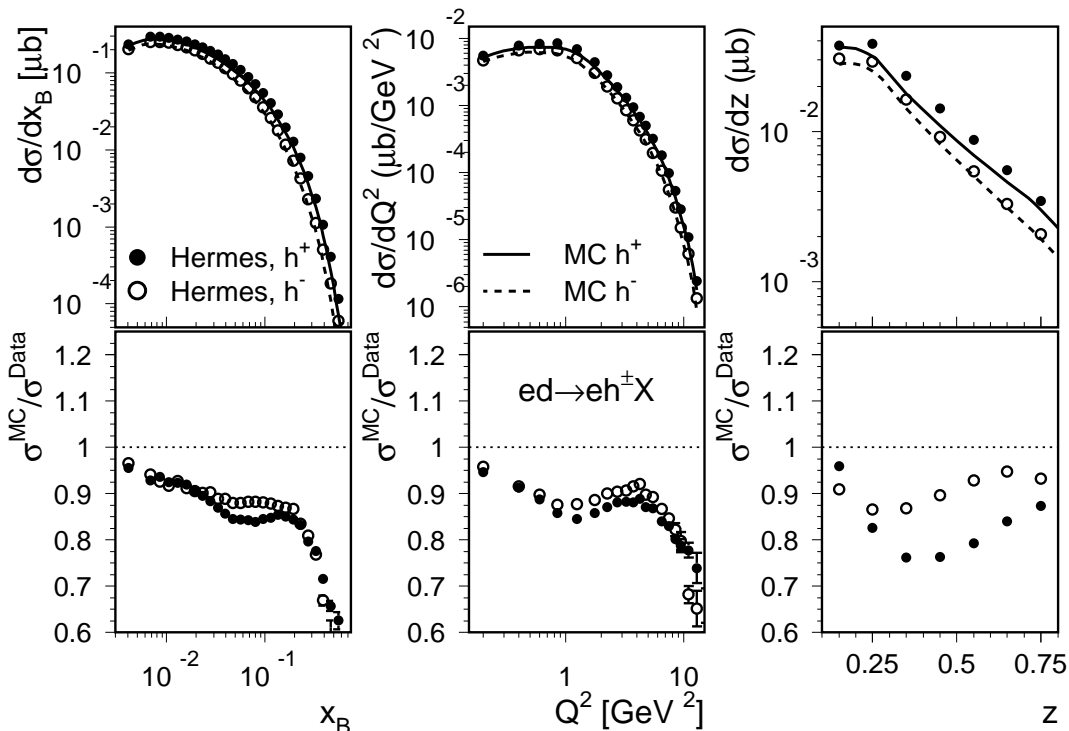
Figure 6: Top panels: Measured cross section in the HERMES acceptance for tagged hadrons as a function of x_B (left), Q^2 (middle), and z (right) for positive (full points) and negative hadrons (open points) using a deuterium target. The lines show the tuned PYTHIA 6.2 calculation. Bottom panels: The corresponding ratios of the PYTHIA calculation to the measured cross section.

this region the modified PYTHIA 6.2 program with the adjusted parameters gives a good representation of the cross section at HERMES energies.

The description of the kinematic dependences of the tuned Monte Carlo code for the individual subprocesses must be consistent with independent LO pQCD calculations [67]. Such calculations presently exist only for inclusive π^0 production and only in the collinear approach, where the intrinsic transverse momentum k_T of the partons in the nucleon and in the virtual photon, and also the transverse momentum p_T^{frag} arising from the fragmentation process are set to zero.

For a comparison of PYTHIA with these LO calculations a special simulation with $k_T = 0$ and $p_T^{frag} = 0$ was performed, by replacing the string fragmentation performed by JETSET with weights obtained from the fragmentation functions of Ref. [68]. The resulting transverse momentum $p_{T(beam)}$ of the π^0 is calculated according to $p_{T(beam)} = z \cdot \hat{p}_T$. Both this simulation and the pQCD calculation are performed in the HERMES kinematics for inclusive π^0 production at $Q^2 < 0.01$ GeV^2, $0.2 < y < 0.9$, disregarding the detector acceptance. Figure 7 compares the resulting cross sections for resolved photon, QCDC, and PGF processes from the simulation and the pQCD calculation. In the collinear approach the DIS subprocess is not included, because the $p_{T(\gamma^*)}$ of the final state hadron is zero, and also for low Q^2 ($Q^2 < 0.01$ GeV^2) it does not result in a sizable $p_{T(beam)}$.

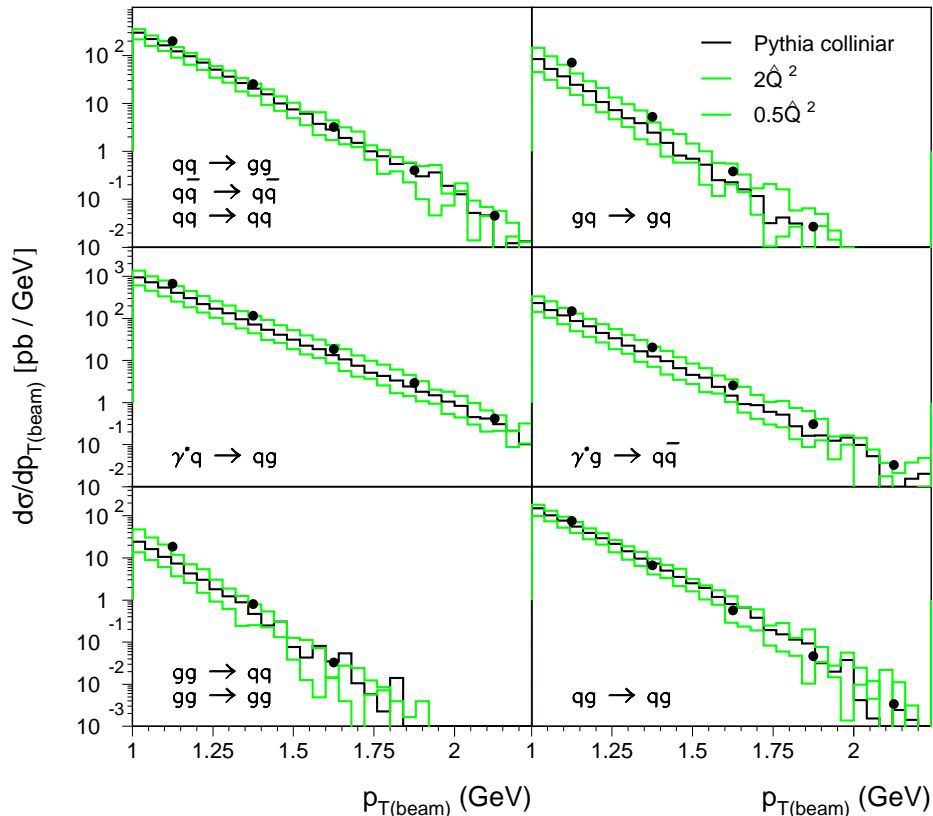The agreement between the simulated cross sections for the individual subprocesses

Figure 7: Cross sections for inclusive π^0 production from resolved photon, QCDC, and PGF processes simulated using PYTHIA (solid lines) compared to the LO pQCD calculations from Ref. [69] (full points). Simulation and calculation are done in the collinear approach at $Q^2 < 0.01$ GeV^2, $0.2 < y < 0.9$. Green/Grey lines: subprocess cross sections after varying the renormalization and factorization scales by factors of $\frac{1}{2}$ and 2 in the simulation.

and the calculations is well within the scale uncertainty $(\frac{1}{2} \hat{Q}^2, 2 \hat{Q}^2)$ of the simulation (the dashed lines in Fig. 7). The LO pQCD calculations show a similar dependence on the variation of the renormalization and factorization scales $(\frac{1}{2} p_{T(beam)}, 2 p_{T(beam)})$, see Fig. 11 in Ref. [67].

5.2 Effects of intrinsic and fragmentation transverse momenta

While the effect of intrinsic and fragmentation transverse momenta cannot yet be studied in LO pQCD calculations, a PYTHIA simulation can be used. For the standard simulations presented in this analysis a Gaussian distribution with a 0.4 GeV width is used for both k_T and p_T^{frag} [66]. These values are consistent with those obtained in Ref. [70]. Both intrinsic and fragmentation transverse momenta alter the relationships of $\hat{p}_T^2$ to $p_{T(beam)}$,

from $p_{T(beam)} = z \cdot \hat{p}_T$ to $p_{T(beam)} = z(k_T + \hat{p}_T) + p_T^{frag}$, and hence the distribution of $\hat{p}_T^2$ and x. This in turn influences the dependence of the cross section on $p_{T(beam)}$. The effects on the cross section for inclusive π^0 production from the PGF subprocess, of first adding nonzero $k_T = 0.4$ GeV and secondly using JETSET with $p_T^{frag} = 0.4$ GeV are shown in Fig. 8. Including only k_T in the simulation decreases $\langle \hat{p}_T^2 \rangle$ from 1.9 GeV^2 to 1.6 GeV^2 and $\langle x \rangle$ from 0.32 to 0.28, and increases the cross section by a factor of two. Including both k_T and p_T^{frag} further decreases $\langle \hat{p}_T^2 \rangle$ to 1.1 GeV^2 and $\langle x \rangle$ to 0.22, and increases the cross section by another factor of 10. These studies show that at fixed-target kinematics, like at HERMES, intrinsic and fragmentation transverse momenta cannot be neglected in pQCDC calculations. Similar conclusions were drawn in Ref. [71]. Perhaps resummation techniques [72], which account for initial and final state radiation effects, can help to achieve more realistic calculations.
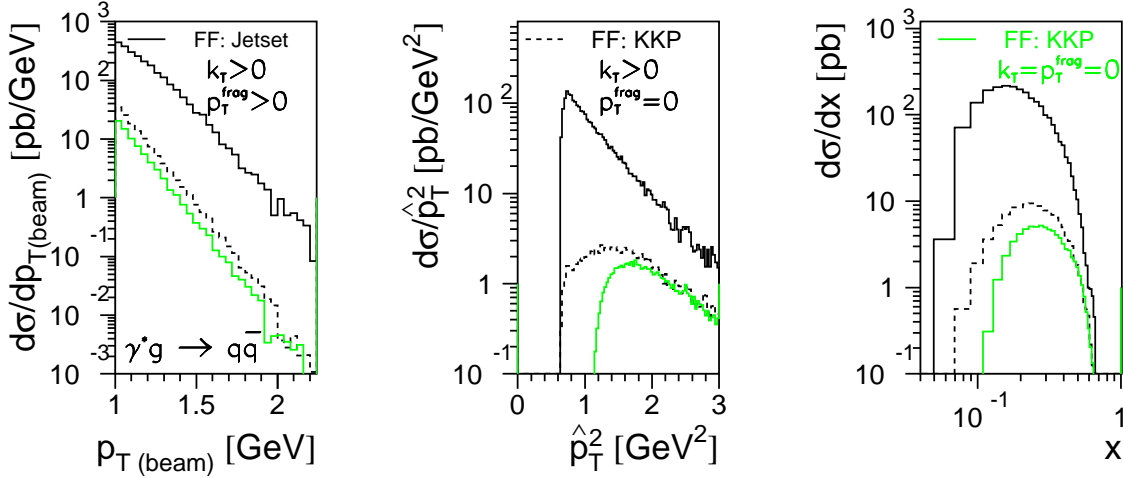

Figure 8: The simulated cross section for inclusive π^0 production from the PGF subprocess vs. $p_{T(beam)}$, $\hat{p}_T^2$, and x for $Q^2 < 0.01$ GeV^2, $0.2 < y < 0.9$. The simulations are done using the collinear approach ((green/gray) solid line), the collinear approach together with intrinsic k_T for the partons in nucleon and photon (dashed line), and with intrinsic k_T together with fragmentation transverse momenta (solid line). For the first two simulations fragmentation is modeled using the KKP-fragmentation functions [68], for the third one JETSET is used.

5.3 Analysis of Monte Carlo events

PYTHIA events are used to calculate cross sections, individual subprocess fractions R_i and event weights $\langle w \rangle_i$ within the HERMES acceptance. The event weights for the pQCD processes (Eq. 4.4) are obtained using the hard subprocess asymmetries (see appendix A) and GRSV (standard scenario) [73] helicity-dependent PDFs in conjunction with the GRV98 [74] helicity-averaged PDFs to calculate $\Delta f^N / f^N$ for the nucleon. In order to calculate $\Delta f^\gamma / f^\gamma$ for the photon the averages of the maximal and minimal scenarios of the GRS [75, 76] helicity-dependent PDFs are used in conjunction with the GRS [77] helicity-averaged PDFs.

For elastic and diffractive VMD processes the asymmetry is set to zero [59]. For the low-p_T process two alternative assumptions for the asymmetry have been investigated: $A_{low\text{-}p_T} = D(y, Q^2) \cdot A_1$ and $A_{low\text{-}p_T} = 0$ where A_1 is a parameterization of the photon-nucleon asymmetry in inclusive DIS. The resulting MC asymmetries and the measured asymmetry are shown in Fig. 9 (left) vs. x_B for the tagged category and a hydrogen target. The corresponding deuterium data are not shown because for this target both assumptions are indistinguishable and match the data. For the anti-tagged category (Fig. 9 (right)) the $p_{T(beam)}$ dependence of the double-spin inclusive asymmetry $A_\parallel$ is shown for both targets. The model $A_{low\text{-}p_T} = D \cdot A_1$ matches the data better than $A_{low\text{-}p_T} = 0$ in the kinematic domains where $R^{low\text{-}p_T}$ is large (low-x_B for tagged and the lowest p_T for anti-tagged categories, respectively) and contributions of hard QCD processes are negligible. The standard asymmetry for the low-p_T process was chosen to be $A_{low\text{-}p_T} = D \cdot A_1$, because of this agreement and because the semi-inclusive asymmetry for all charged hadrons is approximately equal to the measured inclusive asymmetry. The world data on A_1 have been parameterized by $a + x_B^b \cdot (1 - e^{cx_B})$ for $x_B > 10^{-3}$, and extrapolated to the smaller x_B-values ($\langle x_B \rangle \sim 0.0001$) typical for the anti-tagged sample.
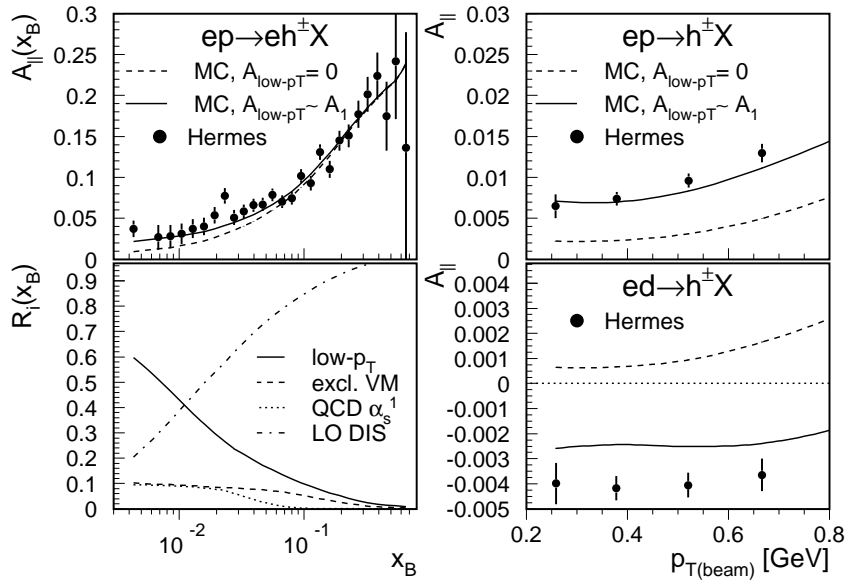

Figure 9: Left panels: The measured double-spin inclusive asymmetry $A_\parallel$ (full points) and two MC asymmetries (solid and dashed lines) based on different assumptions for the low-p_T subprocess asymmetry (top) and the process fractions vs. x_B (bottom) for tagged events on a hydrogen target. Right panels: Double-spin asymmetry vs. $p_{T(beam)}$ for anti-tagged hadrons on a hydrogen (top) and deuterium (bottom) target.

To avoid any bias from the experimental trigger to the results presented, the MC events received an additional weight to account for trigger inefficiencies, if measured and simulated cross sections are compared. The p_T dependences of the cross sections, individual subprocess fractions R_i, average event weights A_i, and weighted asymmetries $R_i A_i$ for the three event categories are shown in Figs. 10 (anti-tagged), 11 (tagged), and 12 (pairs). All three categories have in common that:

- The cross sections span four orders of magnitude, decreasing rapidly with p_T;

- Reasonable agreement between data and Monte Carlo is observed for low transverse momenta. With increasing p_T the Monte Carlo description becomes worse, underestimating the data by up to a factor of four at the largest p_T;

- The fractions R^{low-p_T} and $R^{excl.VMD}$ decrease with increasing p_T and the corresponding asymmetries are very small or zero, respectively;

- In general the contributions from hard QCD subprocesses increase with increasing p_T. At high p_T subprocesses involving quarks in the nucleon contribute less than the signal processes;

- The asymmetries for the two signal subprocesses, QCD $2 \rightarrow 2(g)$ and PGF have opposite sign. For a positive gluon polarization like that of GRSV, this results in a sizable negative asymmetry for PGF, and positive asymmetries for the $2 \rightarrow 2(g)$ processes;

- Some asymmetries and fractions depend on the charge of the hadron.

Even though soft effects from initial and final state radiation and additional nonperturbative processes are taken into account in the Pythia simulation, the Monte Carlo simulation still fails to describe the cross sections at $p_T > 1$ GeV. This shortcoming may be explained by missing large higher order corrections to the hard processes. These corrections have been evaluated for the next to leading order (NLO) cross section in Ref. [67], in the collinear approach for $Q^2 < 0.01$ GeV^2 and $p_T^{col} = z\hat{p}_T > 1$ GeV, for all hard processes (QCD $2 \rightarrow 2$, PGF, QCDC) contributing in this region. The similar kinematics of hard processes in the pQCD-calculation and the PYTHIA simulation allows one to approximate the effect of NLO corrections to the Monte Carlo cross section. A k-factor, $i.e.$, the ratio of LO to NLO cross sections is applied as a weight to each hadron originating from a hard process. The k-factors from Ref. [67] are very large (almost 5) at $p_T \approx 1$ GeV and decrease with p_T to about 2.5 at $p_T = 2.4$ GeV. For the reweighting of the Monte Carlo events they have been extrapolated down to $p_{T(beam)} = 0.8$ GeV, and it was assumed that p_T^{col} can be approximated by $p_{T(beam)}$ (see the discussion in Sect. 5.1 about the collinear approximation). The results shown in the cross section ratio of Fig. 10 indicate that the inclusion of NLO effects to the Monte Carlo could significantly improve the description of the cross section. Effects of similar size may exist for the other categories, but NLO calculations for those are not yet available. The k-factors for the asymmetry have also been calculated in [67] and are approximately 2 in the experimental range. Unfortunately it is not possible to consistently take into account k-factors in the extraction of $\frac{\Delta g}{g}(x, \mu^2)$, therefore the result will essentially be a LO result subject to potentially large NLO corrections.
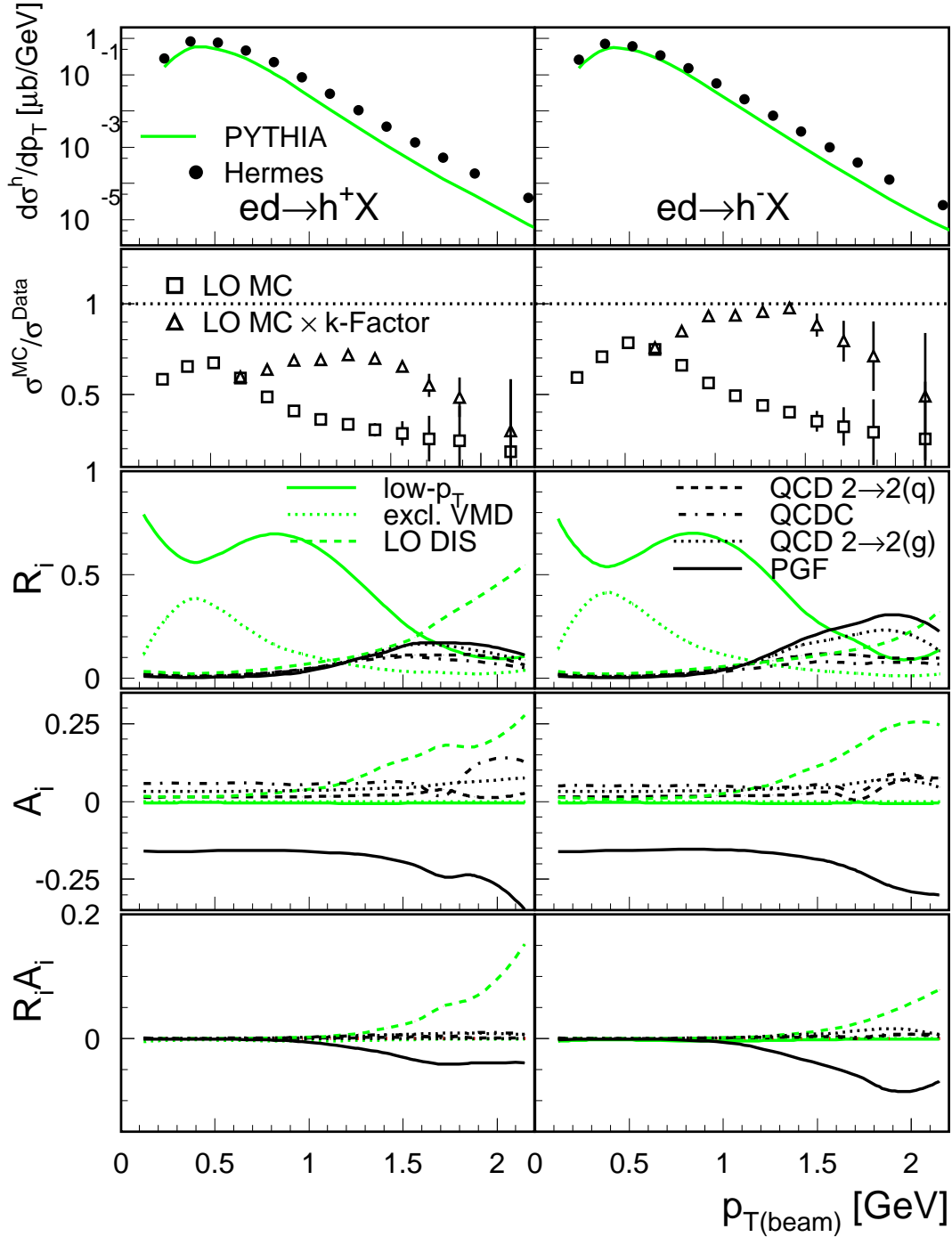
Figure 10: The cross sections and subprocess contributions, in the HERMES acceptance as a function of $p_{T(beam)}$ for the anti-tagged category of events and a deuterium target (left: positively charged hadrons, right: negatively charged hadrons). Top: The measured cross section and that generated by PYTHIA. Second row: The ratio of these two cross sections. Also shown is the effect of the k-factor based on Ref. [67] (see text). Third row: The subprocess fractions from PYTHIA. Bottom two rows: The asymmetries and the asymmetries weighted with the subprocess fractions for each subprocess using Refs. [73] and [74] for the gluon PDFs.
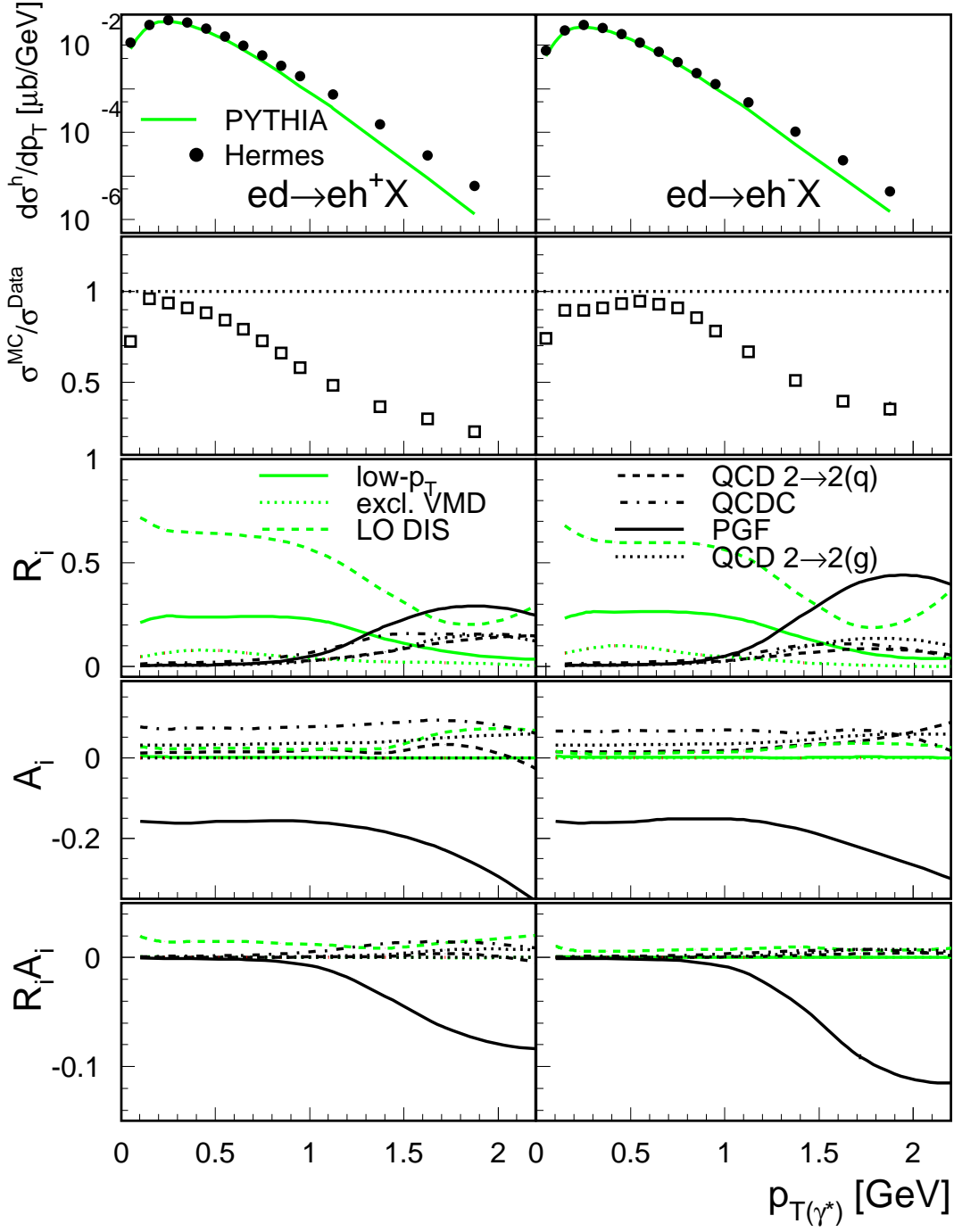
Figure 11: The cross sections and subprocess contributions, in the HERMES acceptance, as a function of $p_{T(\gamma^*)}$ for the tagged category of events and a deuterium target (left: positively charged hadrons, right: negatively charged hadrons). Top: The measured cross section and that generated by PYTHIA. Second row: The ratio of these two cross sections. Third row: The subprocess fractions from PYTHIA. Bottom two rows: The asymmetries and the asymmetries weighted with the subprocess fractions for each subprocess using Refs. [73] and [74] for the gluon PDFs.

Figure 12: The cross sections and subprocess contributions, in the HERMES acceptance, as a function of the minimum value of $\sum p^2_{T(beam)}$ for the production of inclusive hadron pairs on a deuterium target. Top: The measured cross section and that generated by PYTHIA. Second row: The ratio of these two cross sections. Third row: The subprocess fractions from PYTHIA. Bottom two rows: The asymmetries and the asymmetries weighted with the subprocess fractions for each subprocess using Refs. [73] and [74] for the gluon PDFs.
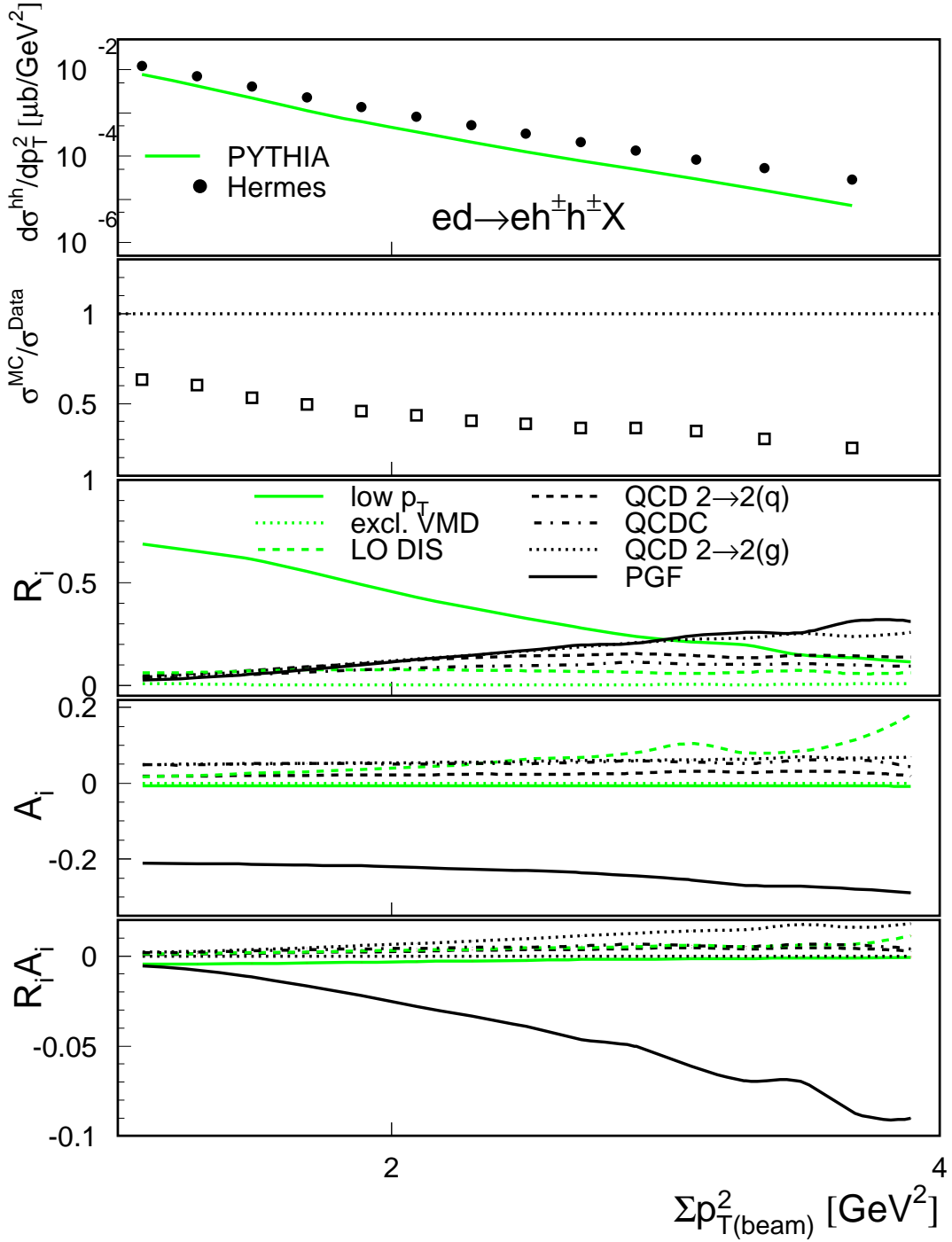
For the anti-tagged category the LO DIS fraction dominates the yield of positive hadrons at high $p_{T(beam)}$. This is due to the subsample of events with the positron having a large scattering angle and missing the HERMES acceptance. The subprocess fractions for LO DIS and QCDC are larger for positive hadrons because of u-quark dominance. Both signal subprocesses contribute approximately 20% to the cross section at high $p_{T(beam)}$. The pairs category has a larger signal fraction than the other categories, but a much smaller number of events. The mixture of the background processes and their contribution to the background asymmetry is different for each category.

6. Determination of the gluon polarization

6.1 Kinematic considerations and requirements

The average value of $\frac{\Delta g}{g}$ in a p_T range is determined directly from Eq. 6.2 (see Sect. 6.2). However, as shown in Fig. 13, there is a large range of x spanned by the data for each p_T range. In order to circumvent this difficulty, the value of $\frac{\Delta g}{g}$ and the appropriate value of x is determined through a minimization procedure using a functional form for $\frac{\Delta g}{g}(x)$ (see Sect. 6.3). The scale dependence of $\frac{\Delta g}{g}$ is neglected because almost all pQCD models are monotonic and vary slowly as a function of μ^2 over the relatively small relevant range. In
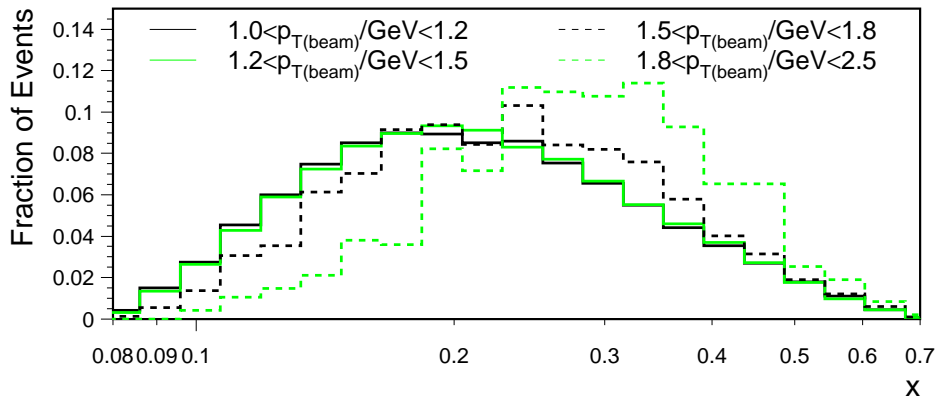

Figure 13: The range of generated x for different values of $p_{T(beam)}$ calculated by PYTHIA for all signal processes, for the anti-tagged category of events and a deuterium target.

order to optimize the accuracy of $\frac{\Delta g}{g}$ the following criteria that maximize the sensitivity of the MC asymmetry to $\frac{\Delta g}{g}$, are applied to the individual data samples:

- 1.0 GeV $<$ $p_{T(\gamma^*)}$ $<$ 2.0 GeV (tagged);
- 1.0 GeV $<$ $p_{T(beam)}$ $<$ 2.5 GeV (anti-tagged);
- 2.0 GeV^2 $<$ $\sum p_T^2$ (pairs).

These requirements balance the statistical accuracy of the measured asymmetries (decreasing with p_T, as shown in Figs. 2-4) against the signal process fractions (increasing with p_T, as shown in Figs. 10-12). For the events within these limits it is observed that:

- The PYTHIA simulations displayed in Fig. 14 show a strong correlation between the hard scattering transverse momentum $\langle \hat{p}_T^2 \rangle$ of the signal subprocesses and the measured hadronic p_T ($\sum p_T^2$);

- For larger values of p_T, there is greater sensitivity to the hard processes involving the gluon (see Figs. 2-4), which leads to reduced systematic uncertainties due to corrections for background asymmetries.
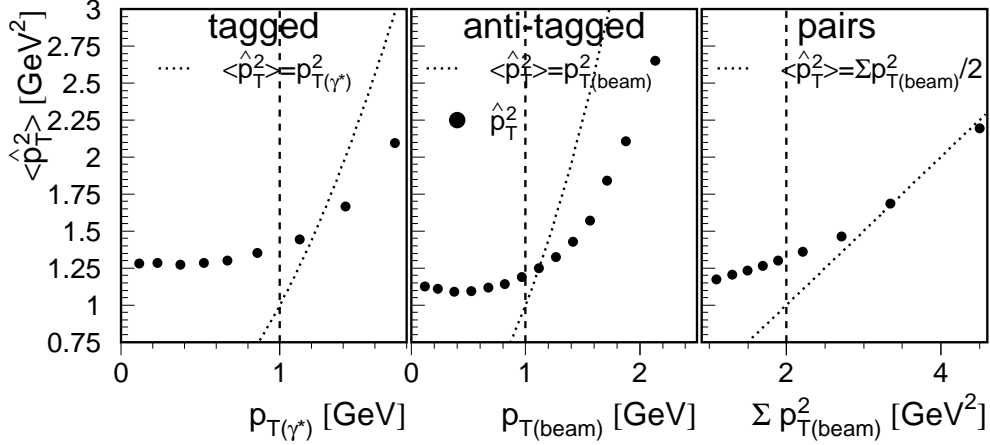

Figure 14: The correlation of the average hard scattering $\langle \hat{p}_T^2 \rangle$ of all signal subprocesses as calculated by PYTHIA with the measured hadron p_T for inclusive hadrons from the deuterium target. Left: tagged category; Center: anti-tagged category; Right: hadron pairs category. The dotted line goes along $\langle \hat{p}_T^2 \rangle = p_T^2(h)$ ($\langle \hat{p}_T^2 \rangle = \sum p_T^2/2$) and the vertical dashed line shows the minimum p_T ($\sum p_T^2$) used for the analysis.

The gluon polarization $\frac{\Delta g}{g}$ is determined using Eqs. 4.3, 4.5, and 4.6. The anti-tagged category has sufficient statistics to allow extraction of $\frac{\Delta g}{g}$ in four $p_{T(beam)}$ bins (1.0 - 1.2 - 1.5 - 1.8 - 2.5 GeV), which are obtained by combining the bins shown in Fig. 2 and table 9. The other categories are represented by a single range in p_T.

6.2 p_T dependence of $\frac{\Delta g}{g}$

If the dependence of $\frac{\Delta g}{g}(x, \mu^2)$ on x and μ^2 is weak in the limited kinematic range of the experiment, $\frac{\Delta g}{g}(x)$ can be factored from the r.h.s of Eqs. 4.5, so that together with Eqs. 4.6 we have

$$
A_{meas}(p_T) - R^{BG} A_{MC}^{BG}(p_T) = \langle \frac{\Delta g}{g} \rangle (p_T) R^{SIG}(p_T) \left\langle \hat{a}(\hat{s}, \hat{t}, \hat{Q}^2, Q^2) \frac{\Delta f_a^{\gamma^*}(x_a, \hat{Q}^2)}{f_a^{\gamma^*}(x_a, \hat{Q}^2)} \right\rangle^{SIG}_{(p_T)}.
$$

(6.1)

Hence the gluon polarization averaged over the covered x and μ^2 ranges can be estimated as

$$
\langle \frac{\Delta g}{g} \rangle (p_T) \equiv \frac{A_{meas}(p_T) - R^{BG} A_{MC}^{BG}(p_T)}{R^{SIG}(p_T) \left\langle \hat{a}(\hat{s}, \hat{t}, \hat{Q}^2, Q^2) \frac{\Delta f_a^{\gamma^*}(x_a, \hat{Q}^2)}{f_a^{\gamma^*}(x_a, \hat{Q}^2)} \right\rangle^{SIG}_{(p_T)}},
$$

(6.2)

where the subprocess fractions and kinematics are determined using PYTHIA. As is shown in Fig. 13, different ranges in p_T correspond to different ranges and distributions in x. It is intrinsic to this method that there is no knowledge on the dependence of $\frac{\Delta g}{g}$ on x, therefore no meaningful value of the average x can be determined by this method, which nevertheless can be used as a consistency check between the different independent data sets.

The results for different event categories, targets and hadron charges are listed in table 4 and shown in Fig. 15 as a function of p_T. The results for the pairs category are displayed at the average $\sqrt{\sum p_T^2/2}$, and those for the tagged category at the average $p_{T(\gamma^*)}$. Each of these data sets has a somewhat different mixture of background and signal processes as a function of p_T, as seen in Figs. 10-12. The measured values of $\langle\frac{\Delta g}{g}\rangle(p_T)$ should be equal for both targets and both hadron charges because of the same range in x and $\hat{Q}^2$. The values shown in Fig. 15 within each category and for each $p_{T(beam)}$ bin indeed agree in general within the statistical uncertainties. This is a strong indication that PYTHIA provides a consistent description of the underlying physics. The systematic charge dependence is accounted for by assigning a systematic uncertainty to the value of the p_T^{frag} (PYTHIA parameter PARJ(21)).
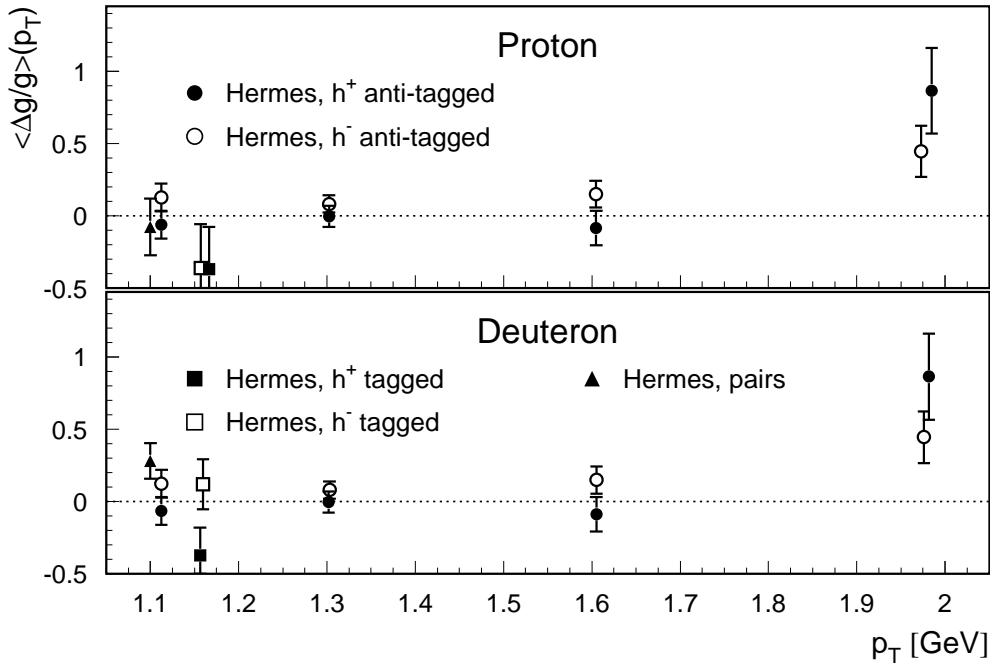

Figure 15: The value of $\langle\frac{\Delta g}{g}\rangle(p_T)$ determined in the anti-tagged category for protons (top) and deuterons (bottom) and positive (full points) and negative (open points) hadrons as a function of p_T. Also shown are the values for the tagged (squares) and pairs (triangle) category at their average respective p_T. The uncertainties shown are statistical only.

6.3 x dependence of $\frac{\Delta g}{g}$

As there is no assumption-free method to determine the average x, various functional forms for $\frac{\Delta g}{g}(x)$ with free parameters were investigated for extracting $\frac{\Delta g}{g}(x)$ from Eqs. 4.5 and 4.6.

	Proton		Deuteron	
$\langle p_T \rangle$ (GeV)	h$^+$	h$^-$	h$^+$	h$^-$
anti-tagged				
1.11	-0.076 ± 0.150	0.201 ± 0.162	-0.063 ± 0.096	0.125 ± 0.096
1.30	0.011 ± 0.120	0.125 ± 0.103	-0.005 ± 0.073	0.080 ± 0.059
1.60	0.116 ± 0.195	0.619 ± 0.174	-0.087 ± 0.119	0.149 ± 0.093
1.98	0.722 ± 0.563	0.154 ± 0.289	0.865 ± 0.297	0.446 ± 0.178
tagged				
1.16	-0.373 ± 0.293	-0.363 ± 0.302	-0.372 ± 0.191	0.119 ± 0.174
pairs				
1.10	-0.079 ± 0.196		0.282 ± 0.122	

Table 4: Results for $\langle \frac{\Delta g}{g} \rangle (p_T)$ for the three categories of events, both targets and hadron charges. Only statistical uncertainties are shown.

Assuming a functional form it is possible to convert the p_T dependence of the asymmetry into a value of $\frac{\Delta g}{g}(x)$ at an average x. In contrast to the method described above, this method works for stronger x dependences of $\frac{\Delta g}{g}$.

For a given functional form and parameter set for $\frac{\Delta g}{g}(x)$ $A_{MC}^{SIG}(p_T)$ can be calculated using Eq. 4.5. The best parameter set is obtained by minimizing the quantity

$$\chi^2 \equiv (\Delta \vec{A})^T C^A \Delta \vec{A}, \tag{6.3}$$

where $\Delta \vec{A}$ is a vector containing the difference between the measured and the calculated asymmetries for each bin in p_T

$$\Delta \vec{A} = \vec{A}_{meas} - (\vec{R}^{BG} A_{MC}^{BG} + \vec{R}^{SIG} A_{MC}^{SIG}). \tag{6.4}$$

The matrix C^A in Eq. 6.3 is the covariance matrix including the statistical uncertainties of the data and MC asymmetries.

A scan over an appropriately large parameter space is performed in order to find the parameters of the function describing $\frac{\Delta g}{g}(x)$ that minimize χ^2. Their covariance matrix C^F is determined from the distribution of probabilities P_k at each scan point k:

$$C_{ij}^F = \frac{\sum_k (\theta_{ik} - \theta_i^{max}) \left(\theta_{jk} - \theta_j^{max} \right) P_k}{\sum_k P_k}. \tag{6.5}$$

In this expression, θ_{ik} is the value of parameter i at point k, while θ_i^{max} is the value of parameter i with the maximum probability. The probabilities P_k can be evaluated from the χ^2 cumulative distribution function. The advantage of this scan procedure is that it ensures finding the *global* minimum and enables the determination of the average x of the measurement using the extracted shape of $\frac{\Delta g}{g}$.

This determination of $\frac{\Delta g}{g}(x)$ can be done only for the anti-tagged category because of the necessity of having several bins in p_T. In order to satisfy the fundamental requirement

for $\frac{\Delta g}{g}(x)$ to vanish at $x = 0$ the functions are required to behave asymptotically as $\frac{\Delta g}{g}(x) \to$ x as $x \to 0$. In addition, $\lim\limits_{x \to 1} \dfrac{\Delta g}{g}(x) \to 1$ was required [78]. Omitting this constraint does not significantly change the results. The small number of $p_{T(beam)}$ bins available limits the choice of the functional forms to those with no more than two free parameters. Several functional forms were studied, and the following two selected:

fct. 1: $x(1 + p_1(1 - x)^2)$,

fct. 2: $x(1 + p_1(1 - x)^2 + p_2(1 - x)^3)$.

The parameters are restricted such that the LO positivity constraint: $|\frac{\Delta g}{g}(x)| < 1$ is satisfied. Figure 16 compares the p_T dependence of the measured asymmetry with the
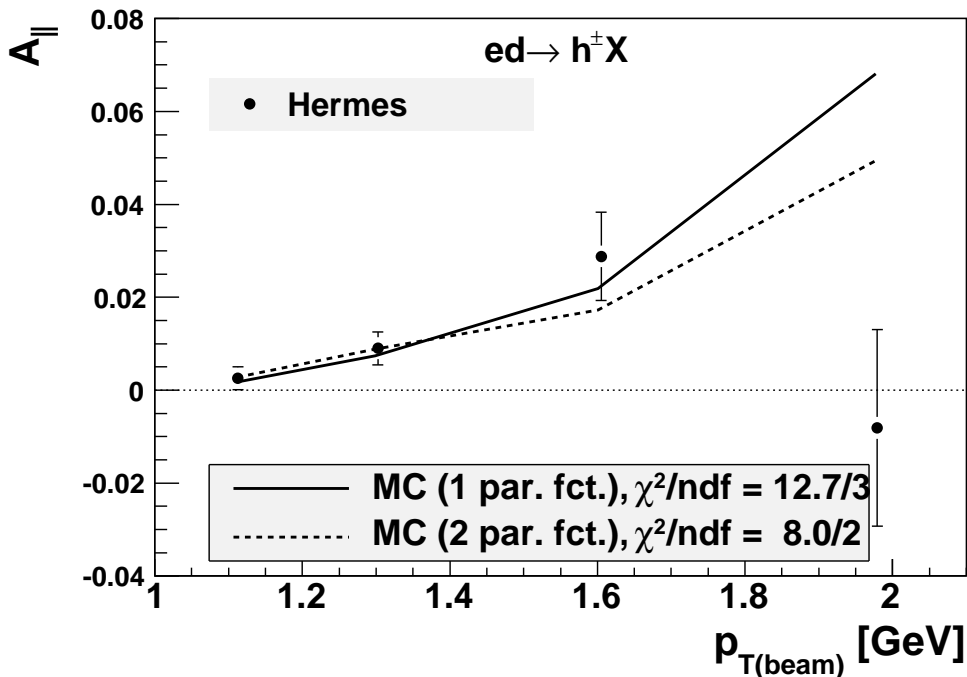

Figure 16: Measured asymmetries with statistical uncertainties in four p_T bins for the anti-tagged category and a deuterium target, compared to calculated asymmetries using the two functions.

asymmetry calculated using the functional forms fitted to the measured asymmetries using Eqs. 4.3 and 4.5. The χ^2 per degree of freedom is large for both functions because of the discrepancy between the measured and calculated asymmetries in the highest p_T bin. No functional form was found that also accommodates the fourth data point within the statistical uncertainty. Systematic uncertainties of the Monte Carlo simulation (see Sect. 6.4) have not been used in this minimization; including them would reduce the χ^2 value significantly.

Figure 17 shows the two functional forms of $\frac{\Delta g}{g}(x)$ and their statistical uncertainties. The parameter value and uncertainties for fct. 1 are given in table 5. The light shaded area represents the full x range spanned by the data, $0.06 < x < 0.7$ (see Fig. 13). The dark shaded area represents the range of x spanned by preponderance of the data as seen
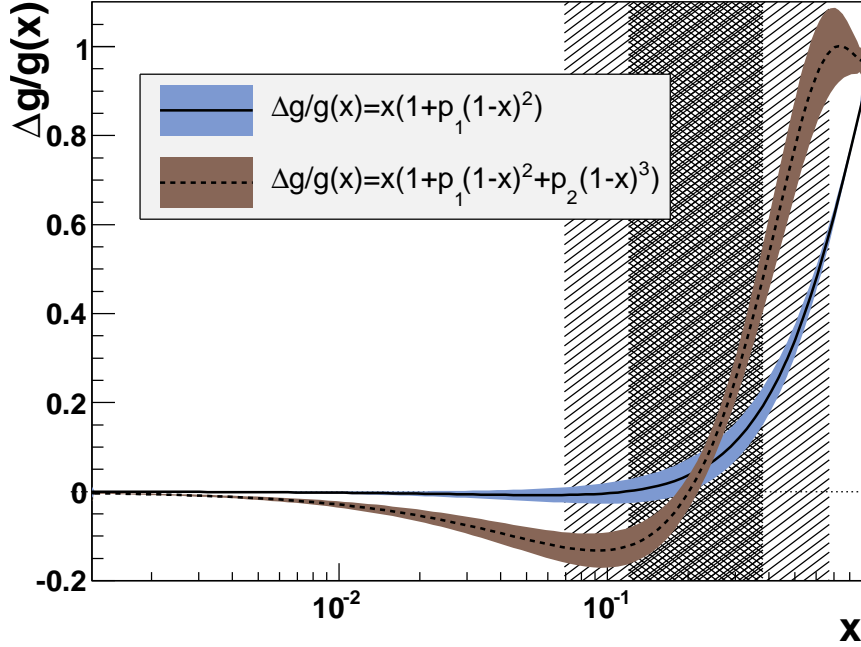
Figure 17: Functional forms used with the values and statistical uncertainty bands from the fits. Light shaded area: the total x range spanned by the data (see Fig. 13); dark shaded area: the range in x where the preponderance of the data lies.

in Fig. 13. Although there are considerable differences in the $\frac{\Delta g}{g}(x)$ functional forms over the full x range, the resulting Monte Carlo asymmetries are not very different, as can be seen from Fig. 16. From the behavior of the measured asymmetries together with the variation of the x-distribution (see Fig. 13) with $p_{T(beam)}$ it can be seen that any smooth function that describes the data leads to $\frac{\Delta g}{g}(x)$ for $x < 0.2$ either small and positive or slightly negative, and significantly positive at larger x. However, no function with so few parameters is able to describe the sudden change of $\frac{\Delta g}{g}(x)$ at $x \approx 0.2$ required to match the measured asymmetry in the largest $p_{T(beam)}$ bin. The average $\frac{\Delta g}{g}$ is determined using the resulting $\frac{\Delta g}{g}(x)$

$$\langle\frac{\Delta g}{g}\rangle \equiv \frac{\Delta g}{g}(\langle x \rangle) = \frac{\displaystyle\sum_{k=1}^{N^{SIG}} \hat{a}_k(\hat{s},\hat{t},\hat{Q}^2,Q^2)\frac{\Delta f_a^{\gamma^*}(x_a^k,\hat{Q}^2)}{f_a^{\gamma^*}(x_a^k,\hat{Q}^2)}\frac{\Delta g}{g}(x^k)}{\displaystyle\sum_{k=1}^{N^{SIG}} \hat{a}_k(\hat{s},\hat{t},\hat{Q}^2,Q^2)\frac{\Delta f_a^{\gamma^*}(x_a^k,\hat{Q}^2)}{f_a^{\gamma^*}(x_a^k,\hat{Q}^2)}} \ , \tag{6.6}$$

where the sum is over all MC hadrons k in the p_T range 1 GeV $< p_T <$ 2.5 GeV. This average determines the average $\langle x \rangle$ of the distribution probed by this measurement using the mean value theorem for integration, i.e., $\langle x \rangle$ is the value of x at which $\langle\frac{\Delta g}{g}\rangle \equiv \frac{\Delta g}{g}(\langle x \rangle)$.

Figure 18 shows the result for $\frac{\Delta g}{g}(x)$ evaluated with fct. 1 in the p_T range 1.0 GeV $< p_T <$ 2.5 GeV and $\frac{\Delta g}{g}(\langle x \rangle)$. The difference between fct. 1 and fct. 2 is assigned as an additional systematic uncertainty on the results from fct. 1 included in $sys - models$ (see
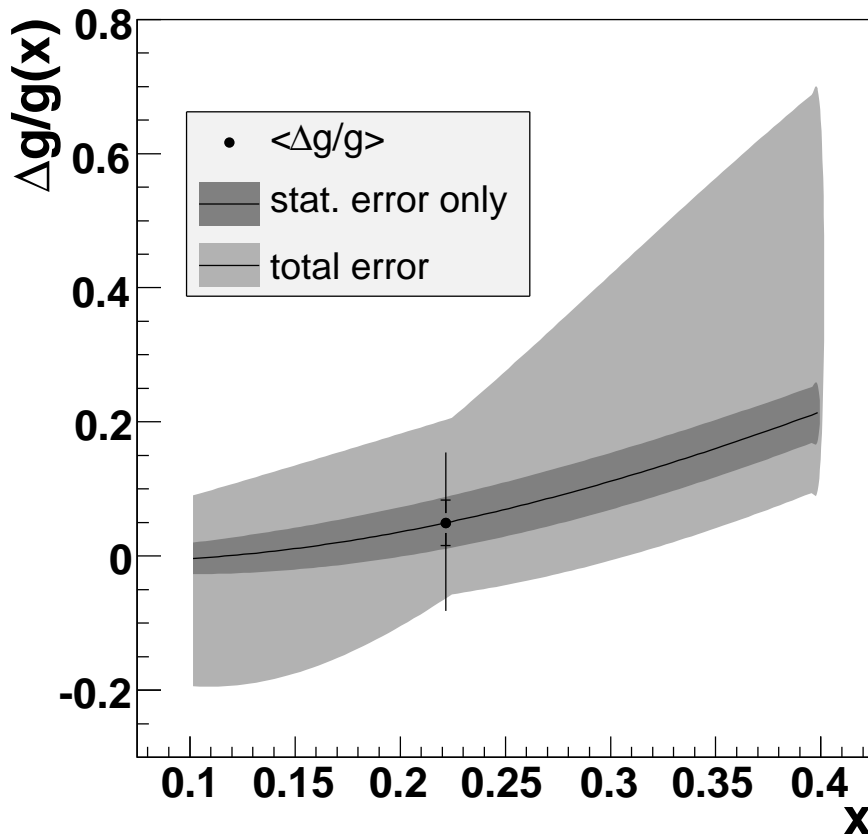
Figure 18: The result for $\frac{\Delta g}{g}(x)$ with fct. 1 vs. x. The point shown represents $\frac{\Delta g}{g}(\langle x \rangle)$ at $\langle x \rangle = 0.22$. The inner error bar / band represents the statistical uncertainty and the outer the total uncertainty obtained by adding statistical and systematic uncertainties in quadrature.

Sect. 6.4). The values of $\langle x \rangle$ determined from the two functions differ by only 0.007.

The value for the gluon polarization extracted for the anti-tagged category from the deuterium target at $\langle x \rangle = 0.22$ and a scale $\langle \mu^2 \rangle = 1.35$ GeV^2 is

$$\frac{\Delta \mathbf{g}}{\mathbf{g}}(\langle \mathbf{x} \rangle) = \mathbf{0.049} \pm \mathbf{0.034(stat)} \pm \mathbf{0.010(sys\text{-}exp)}^{+\mathbf{0.126}}_{-\mathbf{0.099}}(\mathbf{sys\text{-}models}).$$

The scale $\langle \mu^2 \rangle$ was determined by averaging over the scale of all signal MC events. The details on the systematic uncertainties are listed in table 5.

6.4 Systematic uncertainties of $\frac{\Delta g}{g}$

6.4.1 Pythia, Jetset, and helicity-dependent (averaged) PDFs

At present there is no Monte Carlo code available beyond leading order that models all subprocesses relevant at the kinematics of this experiment. Therefore this analysis is limited to leading order. As explained in Sect. 5.1, the Pythia model was significantly improved to better describe the Hermes helicity-averaged data over a wide kinematic range. The model contributions to the systematic uncertainty ('$sys - models$') are determined by varying the parameters controlling the helicity-averaged and helicity-dependent PDFs, the Pythia subprocess cross sections and Jetset fragmentation process, and the low-p_T asymmetry. An individual uncertainty contribution is determined as the difference between

$\frac{\Delta g}{g}$ with the standard setting and $\frac{\Delta g}{g}$ obtained with the alternate setting. Related types of uncertainties are grouped in classes: 'parton distribution functions', 'PYTHIA parameters', 'low-p_T asymmetry', and 'fit function fct. 2'. All the individual and combined uncertainties are shown in table 5.

For most types of uncertainties within a class, *e.g.*, helicity-dependent nucleon PDFs, the uncertainty is conservatively estimated to be the maximum deviation appearing among the alternative models tested. Within a class these maximum differences are added in quadrature to form the 'Total' uncertainty for each class. The 'Total sys-models' uncertainty is obtained by adding those of all classes linearly, because of the complexity of correlations between them.

Each of the classes investigated is motivated and discussed below.

- Parton distribution functions

  Spin-dependent nucleon PDFs

  The alternative parameterizations to GRSV, which were used are: GS-B [79], BB-06 [80], which includes the most recent g_1 data from Refs. [2, 17], and the GRSV standard scenario [73]. The GS-B and BB-06 parameterizations result in deviations, which are the second largest systematic uncertainty. They are of opposite sign and similar magnitude. The third alternative has a negligible effect.

  Spin-dependent photon PDFs

  Alternative parameterizations chosen are the maximum and minimum scenarios of GRS [75, 76]. The resulting deviations are of opposite sign and similar magnitude and make a significant contribution to the overall uncertainty.

  Spin-averaged nucleon PDFs

  Using the alternative parameterization GRV98 [74] results in a small deviation.

  Spin-averaged photon PDFs

  The alternative parameterization is GRS [77], which results in a small deviation.

- PYTHIA parameters

  According to the discussion in Sect. 5.2 the following PYTHIA and JETSET parameters have been varied around their central values: PARP(91) and PARP(99), respectively the initial k_T of the partons in the nucleon and photon, are varied together; PARJ(21), which regulates p_T^{frag}, where the upper and lower values correspond to an increase of χ^2_{std} by 1 unit with respect to the standard setting [66]; PARP(34), which is the multiplicative factor for the factorization and renormalization scales (PARP(34) $\hat{Q}^2$). The scale in the calculation of the asymmetries was varied accordingly. In order to vary the subprocess fractions directly PARP(90) was varied. It is a parameter regulating the cutoff $p_{T_{min}} = PARP(81) \left(\frac{W}{PARP(89)} \right)^{PARP(90)}$ between direct and anomalous processes as well as soft and hard GVMD processes.

  The combined uncertainty of this class is comparable to that from the PDFs class, with PARJ(21) being the largest single contribution.

- Low-p_T asymmetry

  The logical alternative to $A_{low-p_T} = D \cdot A_1$ (which fits the HERMES low-p_T data)

is to assume that at low p_T any spin dependence is washed out, *e.g.*, $A_{low-p_T} = 0$. Any such reduction of the asymmetry would only affect the lowest two p_T bins and could only increase $\frac{\Delta g}{g}$.

- Fit function fct. 2
  For the x dependence, there is an additional class corresponding to functions with the shape of fct. 2.

6.4.2 Experimental systematics

The experimental systematic uncertainty is dominated by the fractional uncertainties in beam and target polarization, as shown in table 1. They are added in quadrature and amount to 3.9% for the asymmetry and 20% for $\frac{\Delta g}{g}(\langle x \rangle)$ from the deuterium target (shown in tables 5 and 8).

Due to the rapid reversal of the target spin orientation (≈ 90 s) the asymmetry extraction is independent of detector efficiency fluctuations. Possible false asymmetries due to the luminosity normalization are found to be negligible.

6.5 Comparison to world data and models

Only a few results obtained in leptoproduction exist on $\frac{\Delta g}{g}$ at present [26, 30, 31, 32]. They were obtained from experiments with widely different kinematics and they have different scales $\hat{Q}^2$. Therefore, they cannot be easily compared. Nevertheless, for comparison the measurements are shown together at their respective $\langle x \rangle$ value, neglecting the Q^2 dependence of $\frac{\Delta g}{g}$. The experimental results shown in Fig. 19 are all obtained in leptoproduction, in LO analyses, although for different final states. The HERMES result is plotted with a horizontal bar indicating the half width at half maximum of the x distribution from Fig. 13. Fit function fct. 1 is shown for the full x range spanned by the HERMES data (see Figs. 19 and 17). The statistical precision of the HERMES result is the best currently available. The COMPASS result for high-p_T hadron pairs in the region $Q^2 < 1$ GeV^2 [31] has almost twice the statistical uncertainty but more data has been taken. Concerning the systematic uncertainty the HERMES result is solidly based on varying many parameters of the well-tuned PYTHIA simulation and a comparison of results from several event categories and targets. The other results on $\frac{\Delta g}{g}$ [26, 30, 32] are characterized by much larger statistical uncertainties. Altogether, the presently available experimental information from leptoproduction clearly indicates small values of $\frac{\Delta g}{g}$ over the covered x range. This conclusion is consistent with the most recent results from polarized pp collisions from PHENIX [24] and STAR [25].

Also shown in Fig. 19 is $\frac{\Delta g}{g}(x, \mu^2)$ calculated from two NLO pQCD fits, obtained as the ratio of the helicity-dependent PDFs (DSSV [6], and BB-09 [81]) to the helicity-averaged PDFs (MRST02 [82] and DR-09 [83], respectively). The BB-09 NLO pQCD fit is based on the inclusive DIS world data set. The DSSV NLO pQCD fit includes the world data on inclusive, semi-inclusive DIS and polarised proton proton scattering. The existing data obtained in leptoproduction on $\frac{\Delta g}{g}(x)$ disfavor large magnitudes of the gluon polarization over the measured x range, in agreement with NLO-QCD fits by DSSV [6].

Kinematics	$\langle x \rangle$	0.217	
	$\langle \mu^2 \rangle$ (GeV^2)	1.353	
		$\Delta g/g$	p_1
x	value	0.049	-1.283
dependence	statistical uncertainty	0.034	0.083
Systematic Uncertainties			
Category	Model	$\delta(\Delta g/g)$	$\delta p1$
helicity-dependent	BB-06	0.029	0.250
Nucleon PDF	GS-B	0.007	0.055
	GRSV-val	0.006	0.055
helicity-dependent	GRV(max)	0.024	0.245
Photon PDF	GRV(min)	-0.019	-0.195
Nucleon PDF	GRV98	-0.005	-0.150
Photon PDF	GRS	0.004	0.055
PYTHIA	PARP(90)=0.14	-0.017	-0.140
parameters	PARP(90)=0.18	0.007	0.040
	PARP(91/99)=0.36	0.002	0.010
	PARP(91/99)=0.44	-0.004	-0.025
	PARJ(21)=0.38	0.021	0.170
	PARJ(21)=0.42	-0.035	-0.290
	PARP(34)=0.5	-0.014	-0.170
	PARP(34)=2.0	0.016	0.170
low-p_T asymmetry		0.046	0.395
Total PDFs $\pm$		0.038	0.385
Total PYTHIA $\pm$		0.042	0.365
fit function fct. 2		-0.018	
Total sys-models $+$		0.126	1.145
Total sys-models $-$		0.099	0.749
Experimental Systematic		0.010	0.040

Table 5: Average kinematics and results for $\frac{\Delta g}{g}(x)$ and the parameter p_1 for fct. 1 with their statistical and systematic uncertainties, from deuteron data for anti-tagged events and for the full range in p_T. For most types of uncertainties within a class, *e.g.*, helicity-dependent nucleon PDFs, the uncertainty is conservatively estimated to be the maximum deviation appearing among the alternative models tested. Within a class (separated box),these maximum differences are added in quadrature to form the 'Total' uncertainty for each class, and referred to as 'Total PDFs' and 'Total PYTHIA'. These components, the 'low-p_T asymmetry' and the 'fit function fct. 2' uncertainties are added linearly to form the 'Total sys-models' uncertainty.

7. Summary

The gluon polarization in the nucleon has been determined by measuring the longitudinal double-spin asymmetry of high-p_T electro-produced single inclusive hadrons at HER-
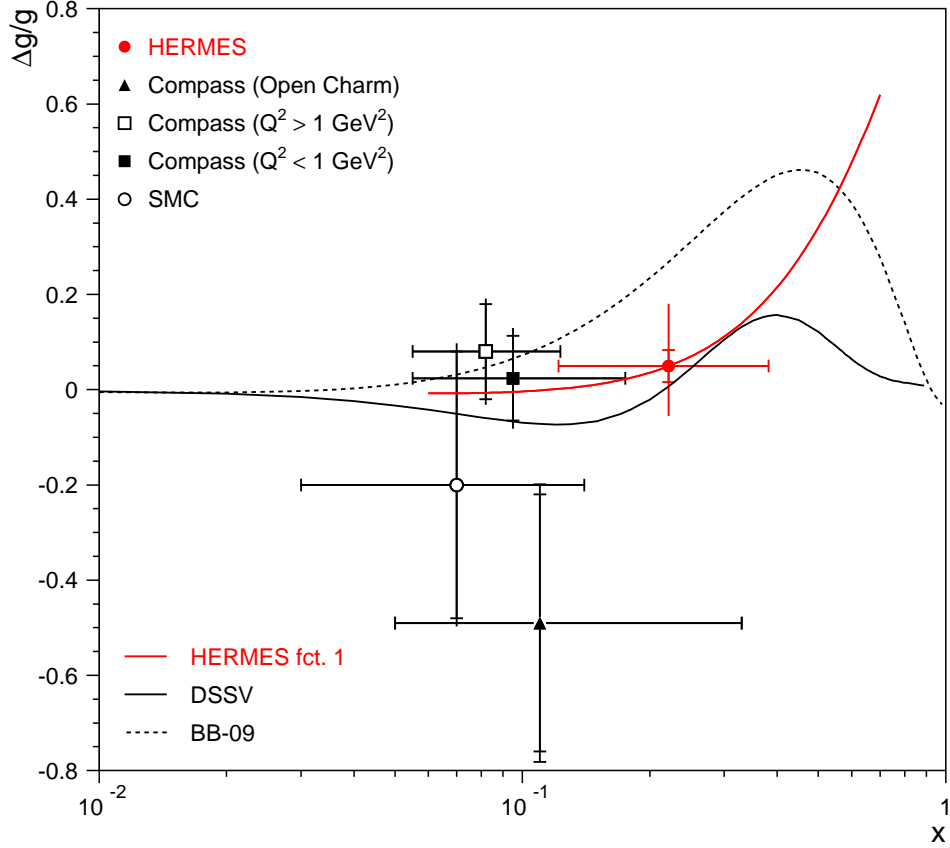
Figure 19: The gluon polarization $\frac{\Delta g}{g}(x)$ from Hermes (fct. 1) ($\mu^2 = 1.35\,\mathrm{GeV}^2$) compared to the ones from Compass [31, 32, 26] (low Q^2: $\mu^2 = 3\,\mathrm{GeV}^2$, high Q^2: $\mu^2 = 2.4\,\mathrm{GeV}^2$, open charm: $\mu^2 = 13\,\mathrm{GeV}^2$) and SMC [30] ($\mu^2 = 3.6\,\mathrm{GeV}^2$) including statistical uncertainties (inner error bars) and total uncertainties (outer error bars). The x region of the data is indicated by the horizontal bars. Fit function fct. 1 is shown over the full x range spanned by the Hermes data. Also shown are a sample of curves from NLO pQCD fits DSSV, and BB-09) at $\mu^2 = 1.5\,\mathrm{GeV}^2$. For clarity only the central values are shown.

MES on a deuterium target. The value of $\frac{\Delta g}{g}$ has been extracted using the measured asymmetries along with the subprocesses fractions, asymmetries and kinematics for the signal and background processes calculated using the leading-order Pythia Monte Carlo code. The value of $\frac{\Delta g}{g}$ is obtained from the product of gluon polarization and subprocess asymmetries summed over a wide range in x. The values of $\langle \frac{\Delta g}{g} \rangle(p_T)$ and $\frac{\Delta g}{g}(x)$ were determined independently. The systematic uncertainty was evaluated by varying Pythia parameters and models of background asymmetries. The final result for the average gluon polarization in the p_T range $1.0\,\mathrm{GeV} < p_T < 2.5\,\mathrm{GeV}$ is $\frac{\Delta g}{g}(x, \mu^2) =$

$0.049\pm0.034(stat)\pm0.010(sys\text{-}exp)^{+0.126}_{-0.099}(sys\text{-}models)$ at $\langle x \rangle = 0.22$ and $\langle \mu^2 \rangle = 1.35$ GeV^2.

Acknowledgments

A. Cross section and asymmetries

The leading-order formulas for helicity-dependent and helicity-averaged cross sections for longitudinally polarized virtual photons and partons for PGF, QCDC, DIS [84] and some QCD $2 \rightarrow 2$ subprocess are shown below. These are integrated over the azimuthal angle between the positron scattering plane and the production plane. The hard subprocess asymmetry $(\hat{a})$ is given by

$$\hat{a}(\hat{s}, \hat{t}, \mu^2) = \Delta\hat{\sigma}/(2\hat{\sigma}), \tag{A.1}$$

$$\Delta\hat{\sigma} = \hat{\sigma}^+ - \hat{\sigma}^-, \tag{A.2}$$

$$\hat{\sigma} = (\hat{\sigma}^+ + \hat{\sigma}^-)/2, \tag{A.3}$$

with $(+)$ denoting that both partons have the same helicity and $(-)$ the opposite helicity. The charge of the struck quark is given by e_q in units of the elementary charge. The common factor C is $\frac{4\pi^2\alpha_{em}}{Q^2(1-x)}$.

$$\textbf{DIS}:$$
$$\frac{d^2\hat{\sigma}_L^{eq \rightarrow q}}{d\nu dQ^2} = 0, \tag{A.4}$$

$$\frac{d^2\hat{\sigma}_T^{eq \rightarrow q}}{d\nu dQ^2} = \Gamma C e_q^2 x, \tag{A.5}$$

$$\frac{d^2\Delta\hat{\sigma}^{eq \rightarrow q}}{d\nu dQ^2} = \Gamma C 2 e_q^2 x. \tag{A.6}$$

For PGF and QCDC, there are helicity-averaged transverse and longitudinal, as well as a helicity-dependent transverse hard cross sections, note in the following $d\hat{\sigma}_i \equiv \frac{d^2\hat{\sigma}_i}{d\hat{s}d\hat{t}}$

$$\textbf{PGF}:$$
$$d\hat{\sigma}_L^{\gamma^* g \rightarrow q\bar{q}} = C\frac{\alpha_s e_q^2}{4\pi}\frac{1}{(Q^2+\hat{s})^2}\frac{8Q^2\hat{s}}{(\hat{s}+Q^2)^2}, \tag{A.7}$$

$$d\hat{\sigma}_T^{\gamma^* g \rightarrow q\bar{q}} = C\frac{\alpha_s e_q^2}{4\pi}\frac{1}{(Q^2+\hat{s})^2}\left[\frac{Q^4+\hat{s}^2}{(\hat{s}+Q^2)^2}\frac{\hat{u}^2+\hat{t}^2}{\hat{u}\hat{t}}\right], \tag{A.8}$$

$$d\Delta\hat{\sigma}_T^{\gamma^* g \rightarrow q\bar{q}} = C\frac{\alpha_s e_q^2}{2\pi}\frac{1}{(Q^2+\hat{s})^2}\left[\frac{Q^2-\hat{s}}{\hat{s}+Q^2}\frac{\hat{u}^2+\hat{t}^2}{\hat{u}\hat{t}}\right], \tag{A.9}$$

where $\hat{s} = (p_q+p_{\bar{q}})^2$, $\hat{t} = (q-p_q)^2$, $\hat{u} = (q-p_{\bar{q}})^2$ and $q, p_q, p_{\bar{q}}$ are the 4-momenta of photon, final quark and anti-quark, as shown in Fig. 1b.

$$\textbf{QCDC}:$$
$$d\hat{\sigma}_L^{\gamma^* q \rightarrow qg} = C\frac{2\alpha_s e_q^2}{3\pi}\frac{1}{(Q^2+\hat{s})^2}\frac{4Q^2\hat{u}}{(\hat{s}+Q^2)^2}, \tag{A.10}$$

$$d\hat{\sigma}_T^{\gamma^* q \rightarrow qg} = C\frac{2\alpha_s e_q^2}{3\pi}\frac{1}{(Q^2+\hat{s})^2}\left[2 - \frac{2\hat{u}Q^2}{(\hat{s}+Q^2)^2} - \frac{Q^4+\hat{u}^2}{\hat{s}\hat{t}}\right], \tag{A.11}$$

$$d\Delta\hat{\sigma}_T^{\gamma^* q \rightarrow qg} = C\frac{4\alpha_s e_q^2}{3\pi}\frac{1}{(Q^2+\hat{s})^2}\left[\frac{2(Q^2-\hat{u})}{Q^2+\hat{s}} - \frac{Q^4+\hat{u}^2}{\hat{s}\hat{t}}\right]. \tag{A.12}$$

Reaction	$d\hat{\sigma}/d\hat{t}$	$d\Delta\hat{\sigma}/d\hat{t}$
$qg \to qg$	$(\hat{s}^2+\hat{u}^2)[\frac{1}{\hat{t}^2}-\frac{4}{9\hat{s}\hat{u}}]$	$2(\hat{u}^2-\hat{s}^2)[\frac{4}{9\hat{s}\hat{u}}-\frac{1}{\hat{t}^2}]$
$\bar{q}g \to \bar{q}g$	$(\hat{s}^2+\hat{u}^2)[\frac{1}{\hat{t}^2}-\frac{4}{9\hat{s}\hat{u}}]$	$2(\hat{u}^2-\hat{s}^2)[\frac{4}{9\hat{u}\hat{s}}-\frac{1}{\hat{t}^2}]$
$gg \to q\bar{q}$	$\frac{\hat{u}^2+\hat{t}^2}{6\hat{u}\hat{t}}-\frac{3}{8}\frac{\hat{t}^2+\hat{u}^2}{\hat{s}^2}$	$\frac{3}{4}\frac{\hat{t}^2+\hat{u}^2}{\hat{s}^2}-\frac{\hat{u}^2+\hat{t}^2}{3\hat{u}\hat{t}}$
$gg \to gg$	$\frac{9}{2}(3-\frac{\hat{t}\hat{u}}{\hat{s}^2}-\frac{\hat{s}\hat{u}}{\hat{t}^2}-\frac{\hat{s}\hat{t}}{\hat{u}^2})$	$9(-3+2\frac{\hat{s}^2}{\hat{u}\hat{t}}+\frac{\hat{u}\hat{t}}{\hat{s}^2})$
$q_a q_b \to q_a q_b$	$\frac{4}{9}[\frac{\hat{s}^2+\hat{u}^2}{\hat{t}^2}+\delta_{ab}(\frac{\hat{s}^2+\hat{t}^2}{\hat{u}^2}-\frac{2\hat{s}^2}{3\hat{t}\hat{u}})]$	$\frac{8}{9}[\frac{\hat{s}^2-\hat{u}^2}{\hat{t}^2}-\delta_{ab}(\frac{\hat{t}^2-\hat{s}^2}{\hat{u}^2}+\frac{2\hat{s}^2}{3\hat{t}\hat{u}})]$
$q_a \bar{q}_b \to q_c \bar{q}_d$	$\frac{4}{9}[\delta_{ac}\delta_{bd}\frac{\hat{u}^2}{\hat{t}^2}+\delta_{cd}\delta_{ab}\frac{\hat{t}^2+\hat{u}^2}{\hat{s}^2}-$ $\delta_{ad}\delta_{cd}\frac{2\hat{u}^2}{3\hat{s}\hat{t}}+\delta_{ab}\delta_{bd}\frac{\hat{s}^2}{\hat{t}^2}]$	$\frac{8}{9}[-\delta_{ac}\delta_{bd}\frac{\hat{u}^2}{\hat{t}^2}-\delta_{cd}\delta_{ab}\frac{\hat{t}^2+\hat{u}^2}{\hat{s}^2}+$ $\delta_{ad}\delta_{cd}\frac{2\hat{u}^2}{3\hat{s}\hat{t}}+\delta_{ab}\delta_{bd}\frac{\hat{s}^2}{\hat{t}^2}]$
$q\bar{q} \to gg$	$\frac{32}{27}\frac{\hat{t}^2+\hat{u}^2}{\hat{u}\hat{t}}-\frac{8}{3}\frac{\hat{t}^2+\hat{u}^2}{\hat{s}^2}$	$-\frac{64}{27}\frac{\hat{t}^2+\hat{u}^2}{\hat{u}\hat{t}}+\frac{16}{3}\frac{\hat{t}^2+\hat{u}^2}{\hat{s}^2}$

Table 6: Subprocess differential cross sections $(\Delta)\hat{\sigma}^{ab\to cd}$ for parton-parton interactions. The common factor of $\frac{\pi\alpha_s^2}{\hat{s}^2}$ has been omitted.

For hard QCD $2 \to 2$ processes the formulas [85] relevant in this analysis are given in Tab. 6.

For lepton scattering, the helicity-dependent and helicity-averaged cross sections are given by

$$\frac{d^4\Delta\sigma^{eq\to e'ff}}{d\nu dQ^2 d\hat{s}d\hat{t}} = D\Gamma_T \frac{d^2\Delta\hat{\sigma}_T^{\gamma^* q\to ff}}{d\hat{s}d\hat{t}}, \tag{A.13}$$

$$\frac{d^4\sigma^{eq\to e'ff}}{d\nu dQ^2 d\hat{s}d\hat{t}} = \Gamma_T \left(\frac{d^2\hat{\sigma}_T^{\gamma^* q\to ff}}{d\hat{s}d\hat{t}} + \epsilon \cdot \frac{d^2\hat{\sigma}_L^{\gamma^* q\to ff}}{d\hat{s}d\hat{t}}\right), \tag{A.14}$$

where f stands for a quark, an antiquark or a gluon in the final state and D is the virtual-photon depolarization factor

$$D(y,Q^2) = \frac{y\left[\left(1+\gamma^2 y/2\right)\left(2-y\right)-2y^2 m_e^2/Q^2\right]}{y^2\left(1-2m_e^2/Q^2\right)\left(1+\gamma^2\right)+2(1+R)\left(1-y-\gamma^2 y^2/4\right)}, \tag{A.15}$$

$\gamma^2 = Q^2/\nu^2$, $R = \sigma_L/\sigma_T$ for the subprocess, and Γ_T is the transverse photon flux factor

$$\Gamma_T = \frac{\alpha_{em}(1-x)}{2\pi Q^2 \nu}\left[y^2\left(1-2m_e^2/Q^2\right)+\frac{2\left(1-y-\gamma^2 y^2/4\right)}{1+\gamma^2}\right], \tag{A.16}$$

and

$$\epsilon = \left[1+\frac{1}{2}\left(1-2m_e^2/Q^2\right)\frac{y^2+\gamma^2 y^2}{1-y-\gamma^2 y^2/4}\right]^{-1}. \tag{A.17}$$

B. Tuned PYTHIA parameters

MSEL=2	MSTP(13)=2	MSTP(17)=6	MSTP(20)=4
MSTP(38)=4	MSTP(61)=0	MSTP(71)=0	MSTP(81)=0
MSTP(92)=4	MSTP(101)=1	MSTP(121)=1	
PARP(2)=7	PARP(18)=0.17	PARP(91)=0.40	PARP(93)=2
PARP(99)=0.40	PARP(102)=0.5	PARP(103)=0.5	PARP(104)=0.3
PARP(111)=0	PARP(121)=2	PARP(161)=3.00	PARP(162)=24.6
PARP(163)=18.8	PARP(165)=0.477	PARP(166)=0.676	
PARJ(1)=0.029	PARJ(2)=0.283	PARJ(3)=1.20	PARJ(21)=0.40
PARJ(41)=1.94	PARJ(42)=0.544	PARJ(45)=1.05	
MSTJ(12)=1	MSTJ(45)=4		
MSTU(112)=4	MSTU(113)=4	MSTU(114)=4	
CKIN(1)=1.0	CKIN(65)=$1. \cdot 10^{-9}$	CKIN(66)=100.	

Table 7: The PYTHIA parameters, tuned to HERMES data, which are different from the default settings that can be found in Ref. [49].

C. Systematic Uncertainties

	p_T bin (GeV)	1.0-1.2	1.2-1.5	1.5-1.8	1.8-2.5	1.0-2.5
Kinematics	$\langle p_T \rangle$ (GeV)	1.11	1.30	1.60	1.90	1.20
	Values					
p_T	$\Delta g/g$	0.017	0.033	0.026	0.619	0.055
dependence	$\delta(\Delta g/g)(stat)$	0.067	0.046	0.073	0.154	0.033
	Systematic Uncertainties					
Category	Model	$\delta(\Delta g/g)$				
spin-dependent	BB-06	0.038	0.019	0.026	0.089	0.027
Nucleon PDF	GS-B	-0.030	-0.031	-0.045	-0.104	-0.037
	GRSV-val	0.007	0.005	0.008	0.001	0.006
spin-dependent	GRV(max)	0.027	0.019	0.014	0.060	0.025
Photon PDF	GRV(min)	-0.019	-0.016	-0.013	-0.069	-0.020
Nucleon PDF	GRV98	0.020	-0.008	-0.031	-0.144	-0.006
Photon PDF	GRS	0.029	0.001	-0.018	0.100	0.004
PYTHIA	PARP(90)=0.14	-0.006	-0.017	0.003	-0.076	-0.016
Parameters	PARP(90)=0.18	0.023	-0.006	-0.018	0.014	0.008
	PARP(91/99)=0.36	0.002	-0.002	0.002	-0.058	-0.001
	PARP(91/99)=0.44	0.004	-0.009	0.002	-0.011	-0.002
	PARJ(21)=0.38	0.036	0.018	0.031	0.110	0.021
	PARJ(21)=0.42	-0.023	-0.040	-0.032	-0.072	-0.034
	PARP(34)=0.5	0.017	-0.006	-0.024	-0.187	-0.014
	PARP(34)=2.0	-0.013	0.012	0.012	0.210	0.012
low-p_T asymmetry		0.108	0.037	0.009	0.005	0.046
Total PDFs $\pm$		0.058	0.038	0.059	0.215	0.045
Total PYTHIA$\pm$		0.047	0.038	0.047	0.258	0.033
Total sys-Models $+$		0.212	0.113	0.116	0.473	0.124
Total sys-Models $-$		0.105	0.076	0.107	0.477	0.078
Experimental Systematic		0.003	0.006	0.009	0.002	0.011

Table 8: Average kinematics and results for $\langle \frac{\Delta g}{g} \rangle (p_T)$ with their statistical and systematic uncertainties, from deuteron data for anti-tagged events shown for the four bins and the full range in p_T. For most types of uncertainties within a class, *e.g.*, spin-dependent nucleon PDFs, the uncertainty is conservatively estimated to be the maximum deviation appearing among the alternative models tested. Within a class (separated box), these maximum differences are added in quadrature to form the 'Total' uncertainty for each class, and referred to as 'Total PDFs' and 'Total PYTHIA'. These components and the 'A^{low-p_T}' uncertainties are added linearly into the 'Total sys-Models' uncertainty.

D. Hadron Asymmetries

p_T-bin (GeV)	$\langle p_T \rangle$ (GeV)	deuterium $A^{meas}(h^+)$	$A^{meas}(h^-)$	hydrogen $A^{meas}(h^+)$	$A^{meas}(h^-)$
0.00–0.15	0.12	0.0002 ± 0.0011	-0.0028 ± 0.0011	0.0152 ± 0.0018	0.0109 ± 0.0020
0.15–0.30	0.23	-0.0013 ± 0.0004	-0.0023 ± 0.0004	0.0107 ± 0.0007	0.0081 ± 0.0008
0.30–0.45	0.37	-0.0032 ± 0.0004	-0.0042 ± 0.0004	0.0098 ± 0.0007	0.0080 ± 0.0008
0.45–0.60	0.52	-0.0029 ± 0.0006	-0.0055 ± 0.0006	0.0101 ± 0.0009	0.0095 ± 0.0011
0.60–0.75	0.67	-0.0038 ± 0.0008	-0.0037 ± 0.0009	0.0127 ± 0.0014	0.0119 ± 0.0017
0.75–0.90	0.81	0.0005 ± 0.0012	-0.0027 ± 0.0015	0.0146 ± 0.0021	0.0105 ± 0.0026
0.90–1.05	0.96	-0.0003 ± 0.0019	-0.0007 ± 0.0023	0.0166 ± 0.0033	0.0088 ± 0.0043
1.05–1.20	1.11	0.0069 ± 0.0032	-0.0033 ± 0.0038	0.0351 ± 0.0055	0.0091 ± 0.0071
1.20–1.35	1.26	0.0150 ± 0.0054	-0.0021 ± 0.0063	0.0563 ± 0.0094	0.0167 ± 0.0118
1.35–1.50	1.41	0.0174 ± 0.0091	0.0062 ± 0.0104	0.0487 ± 0.0157	0.0035 ± 0.0197
1.50–1.65	1.56	0.0429 ± 0.0148	-0.0017 ± 0.0172	0.0886 ± 0.0256	-0.0759 ± 0.0327
1.65–1.80	1.71	0.0719 ± 0.0238	-0.0001 ± 0.0277	0.1317 ± 0.0412	-0.0398 ± 0.0530
1.80–2.00	1.88	-0.0075 ± 0.0342	-0.0027 ± 0.0410	0.1605 ± 0.0596	0.0428 ± 0.0776
2.00–2.50	2.16	0.0377 ± 0.0463	-0.0908 ± 0.0572	0.1071 ± 0.0807	0.0575 ± 0.1128
2.50–5.00	3.04	-0.0071 ± 0.0817	0.1201 ± 0.0960	0.0112 ± 0.1405	-0.0102 ± 0.1546

Table 9: Anti-tagged inclusive hadrons: measured longitudinal double-spin asymmetry for positive and negative hadrons on a deuterium (hydrogen) target. The uncertainty shown is statistical only. There is an additional overall normalization uncertainty of 3.9% (5.2%), all other systematic uncertainties are negligible.

p_T-bin (GeV)	$\langle p_T \rangle$ (GeV)	deuterium		hydrogen	
		$A^{meas}(h^+)$	$A^{meas}(h^-)$	$A^{meas}(h^+)$	$A^{meas}(h^-)$
0.00–0.15	0.10	0.0229 ± 0.0045	0.0159 ± 0.0050	0.0896 ± 0.0073	0.0643 ± 0.0089
0.15–0.30	0.23	0.0201 ± 0.0029	0.0120 ± 0.0033	0.0850 ± 0.0048	0.0605 ± 0.0058
0.30–0.45	0.37	0.0188 ± 0.0031	0.0134 ± 0.0036	0.0807 ± 0.0053	0.0479 ± 0.0064
0.45–0.60	0.52	0.0186 ± 0.0040	0.0134 ± 0.0048	0.0789 ± 0.0068	0.0639 ± 0.0085
0.60–0.75	0.67	0.0211 ± 0.0057	0.0066 ± 0.0068	0.0661 ± 0.0095	0.0494 ± 0.0122
0.75–1.00	0.85	0.0104 ± 0.0072	0.0106 ± 0.0088	0.0722 ± 0.0122	0.0683 ± 0.0159
1.00–1.30	1.11	0.0465 ± 0.0143	0.0367 ± 0.0176	0.1055 ± 0.0237	0.1318 ± 0.0314
1.30–1.60	1.40	0.0660 ± 0.0364	-0.0586 ± 0.0431	0.1410 ± 0.0607	0.0481 ± 0.0813
1.60–2.00	1.72	0.0165 ± 0.0903	-0.0390 ± 0.1086	0.0627 ± 0.1501	-0.0229 ± 0.2018
2.00–3.50	2.18	0.1534 ± 0.3059	0.3929 ± 0.3798	-1.5868 ± 0.9548	1.4778 ± 1.4182

Table 10: Tagged inclusive hadrons: measured longitudinal double-spin asymmetry for positive and negative hadrons on a deuterium (hydrogen) target. The uncertainty shown is statistical only. There is an additional overall normalization uncertainty of 3.9% (5.2%), all other systematic uncertainties are negligible.

$(\sum p^2_{T(beam)})_{min}$	$A^{meas}(\text{hh})$	
(GeV^2)	hydrogen	deuterium
1.00	0.023 ± 0.004	-0.005 ± 0.003
1.20	0.018 ± 0.006	-0.005 ± 0.003
1.40	0.016 ± 0.008	-0.000 ± 0.004
1.60	0.031 ± 0.010	0.001 ± 0.006
1.80	0.047 ± 0.013	-0.006 ± 0.007
2.00	0.041 ± 0.016	-0.010 ± 0.009
2.50	0.084 ± 0.028	-0.028 ± 0.015
3.00	-0.001 ± 0.045	-0.041 ± 0.025
4.00	0.042 ± 0.108	-0.080 ± 0.057

Table 11: Inclusive hadron pairs: measured longitudinal double-spin asymmetry for proton and deuterium targets. The uncertainty shown is statistical only. There is an additional overall normalization uncertainty of 5.2% (3.9%) for hydrogen (deuterium), all other systematic uncertainties are negligible.

References

[1] R. Jaffe and A. Manohar, Nucl. Phys. B 337 (1990) 509.

[2] HERMES Collaboration, A. Airapetian, et al., Phys. Rev. D 75 (2007) 012007.

[3] COMPASS Collaboration, V. Y. Alexakhin, et al., Phys. Lett. B 747 (2007) 8.

[4] J. Blümlein, H. Böttcher, Nucl. Phys. B 636 (2002) 225.

[5] AAC Collaboration, M. Hirai, S. Kumano, N. Saito, Phys. Rev. D 74 (2006) 014015.
    AAC Collaboration, M. Hirai, S. Kumano, N. Saito, Phys. Rev. D 69 (2004) 054021.

[6] D. de Florian, R. Sassot, M. Stratmann, W. Vogelsang, Phys. Rev. Lett. 101 (2008) 72001.
    D. de Florian, R. Sassot, M. Stratmann, W. Vogelsang, Phys. Rev. D 80 (2009) 034030.

[7] E. Leader, A. Sidorov, D. Stamenov, Phys. Rev. D 75 (2007) 074027.
    E. Leader, A. Sidorov, D. Stamenov, Phys. Rev. D 73 (2006) 034023.

[8] HERMES Collaboration, A. Airapetian, et al., Phys. Rev. D 71 (2005) 012003.

[9] EMC Collaboration, J. Ashman, et al., Phys. Lett. B 206 (1988) 364.

[10] E142 Collaboration, P. Anthony, et al., Phys. Rev. D 54 (1996) 6620.

[11] HERMES Collaboration, K. Ackerstaff, et al., Phys. Lett. B 404 (1997) 383.

[12] E154 Collaboration, K. Abe, et al., Phys. Rev. Lett. 79 (1997) 26.

[13] SMC Collaboration, B. Adeva, et al., Phys. Rev. D 58 (1998) 112001.

[14] E143 Collaboration, K. Abe, et al., Phys. Rev. D 58 (1998) 112003.

[15] E155 Collaboration, P. L. Anthony, et al., Phys. Lett. B 463 (1999) 339.

[16] E155 Collaboration, P. Anthony, et al., Phys. Lett. B 493 (2000) 19.

[17] COMPASS Collaboration, E. Ageev, et al., Phys. Lett. B 612 (2005) 154.
     COMPASS Collaboration, V. Yu. Alexakhin, et al., Phys. Lett. B 647 (2007) 8.
     COMPASS Collaboration, V. Yu. Alexakhin, et al., Phys. Lett. B 647 (2007) 330.

[18] Hall A Collaboration, X. Zheng, et al., Phys. Rev. Lett 92 (2004) 012004.

[19] W. A. Bardeen, et al., Phys. Rev. D 18 (1978) 3998.

[20] Y. L. Dokshitzer, Sov. Phys. JETP 46 (1977) 641.

[21] V. N. Gribov, L. N. Lipatov, Sov. J. Nucl. Phys. 15 (1972) 438.

[22] G. Altarelli, G. Parisi, Nucl. Phys. B 126 (1977) 298.

[23] E704 Collaboration, D. L. Adams, et al., Phys. Lett. B 261 (1991) 197.

[24] PHENIX Collaboration, S. S. Adler, et al., Phys. Rev. Lett. 93 (2004) 202002.
     PHENIX Collaboration, S. S. Adler, et al., Phys. Rev. D 73 (2006) 091102.
     PHENIX Collaboration, A. Adare, et al., Phys. Rev. D 76 (2007) 051106.
     PHENIX Collaboration, A. Adare, et al., Phys. Rev. Lett. 103 (2009) 012003.
     PHENIX Collaboration, A. Adare, et al., Phys. Rev. D 79 (2009) 012003.

[25] STAR Collaboration, B. I. Abelev, et al., Phys. Rev. Lett. 97 (2006) 252001.
     STAR Collaboration, B. I. Abelev, et al., Phys. Rev. Lett. 100 (2008) 232003.

[26] COMPASS Collaboration, M. Alekseev, et al., hep-ex/0802.3023.
COMPASS Collaboration, M. Alekseev, et al., Phys. Lett. B 676 (2009) 31.

[27] COMPASS Collaboration, P. Abbon, et al., Nucl. Instrum. Meth. A 577 (2007) 455.
COMPASS Collaboration, G. Baum, et al., Common Muon and Proton Apperatus for Structure and Spectroscopy, CERN/SPSLC 96-14 (1996).

[28] E155 Collaboration, P. Anthony, et al., Phys. Lett. B 458 (1999) 536.

[29] HERMES Collaboration, A. Airapetian, et al., Phys. Rev. Lett. 84 (2000) 2584.

[30] SMC Collaboration, B. Adeva, et al., Phys. Rev. D 70 (2004) 012002.

[31] COMPASS Collaboration, E. S. Ageev, et al., Phys. Lett. B 633 (2006) 25.

[32] COMPASS Collaboration, M. Stolarski, Measurements of $\Delta G/G$ from high transverse momentum hadrons pairs in COMPASS, in: Proc. of the 16th International Workshop on Deep Inelastic Scattering and QCD (DIS2008), April 7–April 11, 2008, London, UK, 2008, 209.

[33] P. Liebing, Can the gluon polarization in the nucleon be extracted from HERMES data on single high-p_t hadrons, Ph.D. thesis, Universität Hamburg (2004), DESY-THESIS-2004-036.

[34] V. Mexner, Determination of the gluon polarization in the nucleon, Ph.D. thesis, Universiteit van Amsterdam, (December 2005).

[35] A. Sokolov and I. Ternov, Sov. Phys. Dokladi 8 (1964) 1203.

[36] M. Beckmann, et al., Nucl. Inst. & Meth. A 479 (2002) 334.

[37] D. Barber, et al., Nucl. Inst. & Meth. A 338 (1994) 166.

[38] A. Airapetian, et al., Nucl. Inst. & Meth. A 540 (2005) 68.

[39] A. Nass, et al., Nucl. Inst. & Meth. A 505 (2003) 633.

[40] C. Baumgarten, et al., Nucl. Inst. & Meth. A 482 (2002) 606.

[41] C. Baumgarten, et al., Nucl. Inst. & Meth. A 508 (2003) 268.

[42] T. Benisch, et al., Nucl. Inst. & Meth. A 471 (2001) 314.

[43] HERMES Collaboration, K. Ackerstaff, et al., Nucl. Inst. & Meth. A 417 (1998) 230.

[44] J. Brack, et al., Nucl. Inst. & Meth. A 469 (2001) 47.

[45] A. Andreev, et al., Nucl. Inst. & Meth. A 465 (2001) 482.

[46] N. Akopov, et al., Nucl. Inst. & Meth. A 479 (2002) 511.

[47] S. Bernreuther, et al., Nucl. Inst. & Meth. A 416 (1998) 45.

[48] H. Avakian, et al., Nucl. Inst. & Meth. A 417 (1998) 69.

[49] T. Sjöstrand, L. Lönnbland, S. Mrenna, P. Skands, hep-ph/0108264.

[50] T. Sjöstrand, et al., Comp. Phys. Comm. 135 (2001) 238.

[51] C. Friberg and T. Sjöstrand, JHEP 09 (2000) 010.
C. Friberg, Aspects of qcd and the photon structure, Ph.D. thesis, Lund University (2000).

[52] M. Drees, R. Godbole, J. Phys. G 21 (1995) 1559.

[53] A. Donnachie, P. V. Landshoff, Phys. Lett. B 296 (1992) 227.

[54] G. A. Schuler, T. Sjöstrand, Phys. Lett. B 300 (1993) 169.

[55] G. A. Schuler, T. Sjöstrand, Nucl. Phys. B 407 (1993) 539.

[56] H. Fraas, Nucl. Phys. B 113 (1976) 532.

[57] H. Kochelev, et al., Phys. Rev. D 65 (2002) 097504.

[58] H. Kochelev, et al., Phys. Rev. D 67 (2003) 074014.

[59] HERMES Collaboration, A. Airapetian, et al., Phys. Lett. B 513 (2001) 301.

[60] B. Andersson, The Lund Model, Camb. Monogr. Part. Phys. Nucl. Phys. Cosmol. 7, 1997.

[61] H. Lai, et al., Eur. Phys. J. C 12 (2000) 375.

[62] G. A. Schuler, T. Sjöstrand, Phys. Lett. B 376 (1996) 193.

[63] L. W. Mo, Y. S. Tsai, Rev. Mod. Phys. 41 (1969) 205.

[64] I. Akushevich, H. Böttcher, D. Ryckbosch, hep-ph/9906408.

[65] R. Brun, R. Hagelberg, M. Hansroul, J. Lassalle, CERN-DD-78-2-REV, (1978).

[66] A. Hillenbrand, Measurement and simulation of the fragmentation process at hermes, Ph.D. thesis, Friedrich–Alexander–Universität Erlangen–Nürnberg (2005), DESY-THESIS-2005-035.

[67] B. Jäger, M. Stratmann, W. Vogelsang, Eur. Phys. J. C 44 (2005) 533.

[68] B. A. Kniehl, G. Kramer, B. Pötter, Nucl. Phys. B 582 (2000) 514.

[69] M. Stratmann, Private communication.

[70] M. Anselmino, et al., Phys. Rev. D 71 (2005) 074006.

[71] J. Collins, H. Jung, Need for fully unintegrated parton densities, in: Proceedings of HERA and LHC: A Workshop on the Implications of HERA for LHC Physics, Hamburg, Germany, 21-24 Mar 2005, hep-ph/0508280.

[72] D. de Florian, W. Vogelsang, Phys. Rev. D 71 (2005) 114004.
Y. Koike, J. Nagashima, W. Vogelsang, Nucl. Phys. B 744 (2006) 59.

[73] M. Glück, E. Reya, M. Stratmann, W. Vogelsang, Phys. Rev. D 63 (2001) 094005.

[74] M. Glück, E. Reya, A. Vogt, Eur. Phys. J. C 5 (1998) 461.

[75] M. Glück, E. Reya, C. Sieg, Eur. Phys. J. C 20 (2001) 271.

[76] M. Glück, E. Reya, C. Sieg, Phys. Lett. B 503 (2001) 285.

[77] M. Glück, E. Reya, I. Schienbein, Phys. Rev. D 60 (1999) 054019.

[78] S. Brodsky, M. Burkardt, I. Schmidt, Nucl. Phys. B 441 (1995) 197.

[79] T. Gehrmann, W. J. Stirling, Z. Phys. C 65 (1995) 461.

[80] J. Blümlein, H. Böttcher private communication.

[81] J. Blümlein, H. Böttcher DESY 09-131.

[82] A. D. Martin, R. G. Roberts, W. J. Stirling, and R. S. Thorne, Eur. Phys. J. C 28 (2003) 455.

[83] P. Jimenez-Delgado and E. Reya, Phys. Rev. D 79 (2009) 074023.

[84] A. Bravar, K. Kurek, R. Windmolders, Comput. Phys. Commun. 105 (1997) 42.

[85] J. Babcock, E. Monsay, D. W. Sivers, Phys. Rev. D 19 (1979) 1483.